American Mineralogist, Volume 85, pages 153–172, 2000

Oxidation-reduction mechanism of iron in dioctahedral smectites: II. Crystal chemistry of reduced Garfield nontronite

A. MANCEAU,[1,*] V.A. DRITS,[1,†] B. LANSON,[1] D. CHATEIGNER,[2] J. WU,[3] D. HUO,[3] W.P. GATES,[3,‡,§] AND J.W. STUCKI[3]

[1]Environmental Geochemistry Group, LGIT-IRIGM, University Joseph Fourier and CNRS, 38041 Grenoble Cedex 9, France
[2]LPEC, Université du Maine-Le Mans, av. Olivier Messiaen, BP535 72085 Le Mans cedex, France
[3]Department of Natural Resources and Environmental Sciences, University of Illinois, W-317 Turner Hall, 1102 South Goodwin Avenue, Urbana, Illinois 61801, U.S.A.

ABSTRACT

The crystallochemical structure of reduced Garfield nontronite was studied by X-ray absorption pre-edge and infrared (IR) spectroscopy, powder X-ray diffraction, polarized extended X-ray absorption fine structure (P-EXAFS) spectroscopy, and texture goniometry. Untreated and highly reduced (>99% of total Fe as Fe^{2+}) nontronite samples were analyzed to determine the coordination number and the crystallographic site occupation of Fe^{2+}, changes in in-plane and out-of-plane layer structure and mid-range order between Fe centers, and to monitor the changes in structural and adsorbed OH/H_2O groups in the structure of reduced nontronite. Contrary to earlier models predicting the formation of fivefold coordinated Fe in the structure of nontronites upon reduction, these new results revealed that Fe maintains sixfold coordination after complete reduction. In-plane P-EXAFS evidence indicates that some of the Fe atoms occupy trans-sites in the reduced state, forming small trioctahedral domains within the structure of reduced nontronite. Migration of Fe from cis- to trans sites during the reduction process was corroborated by simulations of X-ray diffraction patterns which revealed that about 28% of Fe^{2+} cations exist in trans sites of the reduced nontronite, rather than fully cis occupied, as in oxidized nontronite. Out-of-plane P-EXAFS results indicated that the reduction of Fe suppressed basal oxygen corrugation typical of dioctahedral smectites, and resulted in a flat basal surface which is characteristic of trioctahedral layer silicates. IR spectra of reduced nontronite revealed that the dioctahedral nature of the nontronite was lost and a band near 3623 cm^{-1} formed, which is thought to be associated with trioctahedral $[Fe^{2+}]_3OH$ stretching vibrations. On the basis of these results, a structural model for the reduction mechanism of Fe^{3+} to Fe^{2+} in Garfield nontronite is proposed that satisfies all structural data currently available. The migration of reduced Fe ions from cis-octahedra to adjacent trans-octahedra is accompanied by a dehydroxylation reaction due to the protonation of OH groups initially coordinated to Fe. This structural modification results in the formation of trioctahedral Fe^{2+} clusters separated by clusters of vacancies in which the oxygen ligands residing at the boundary between trioctahedral and vacancy domains are greatly coordination undersaturated. The charge of these O atoms is compensated by the incorporation of protons, and by the displacement of Fe^{2+} atoms from their ideal octahedral position toward the edges of trioctahedral clusters, thus accounting for the incoherency of the Fe-Fe1 and Fe-Fe2 distances. From these results, the ideal structural formula of reduced Garfield nontronite is $Na_{1.30}[Si_{7.22}Al_{0.78}][Fe^{2+}_{3.65}Al_{0.32}Mg_{0.04}]O_{17.93}(OH)_5$ in which the increased layer charge due to reduction of Fe^{3+} to Fe^{2+} is satisfied by the incorporation of protons and interlayer Na.

INTRODUCTION

Reduction-oxidation reactions of layer silicates in soils and sediments influence environmental processes such as weathering, microbial activity, and diagenetic transformations (Egashira and Ohtsubo 1983; Ernstsen 1998; Stucki et al. 1987). Both physical and chemical properties of smectites are modified by the reduction of structural Fe^{3+}, including cation exchange capacity (Stucki et al. 1984), specific surface area (Lear and Stucki 1985), swelling behavior (Gates et al. 1993; Lear and Stucki 1989), and texture (Gates et al. 1998; Stucki and Tessier 1991). Although we can predict to some extent the effect of Fe oxidation state on smectite chemical and physical properties, we do not know how the surface properties of reduced smectite are controlled due to the lack of molecular level understanding of the reduction mechanism of Fe^{3+}. The present study examines the chemical and structural environment of octahedral Fe in

*E-mail: Alain.Manceau@obs.ujf-grenoble.fr
†And Geological Institute of the Russian Academy of Sciences, 7 Pyzhevsky Street, 109017 Moscow, Russia.
‡And Environmental Geochemistry Group, Grenoble.
§Present address: CSIRO Land and Water, Private Mail Bag No. 2, Glen Osmond, SA 5064, Australia

reduced Garfield nontronite through polarized extended X-ray absorption fine structure (P-EXAFS) spectroscopy, X-ray absorption pre-edge and infrared (IR) spectroscopy, X-ray diffraction (XRD), and texture goniometry, and develops a structural model which accounts quantitatively for the changes of physico-chemical properties described in the literature.

EXPERIMENTAL METHODS

Reduction

The Na-exchanged Garfield nontronite (R. Glaeser), has a structural formula of $[Na_{0.81}(Si_{7.22}Al_{0.78})(Fe^{3+}_{3.64}Fe^{2+}_{0.01}Al_{0.32}Mg_{0.04})O_{20}(OH)_4$ (Table 2 in Manceau et al. 2000). Samples were reduced with Na dithionite following modifications of the method of Komadel and Stucki (1988). Samples (65 mg) were suspended in 10 ml deionized Milli-Q water, to which 30 mL of a citrate-bicarbonate (CB) buffer (1 part 1 *M* $NaHCO_3$:8 parts 0.3 *M* $Na_3C_6H_5O_7$ $2H_2O$) were then added. Then 200 mg solid powder Na-dithionite ($Na_2S_2O_4$) was added to the clay suspension and the reaction was allowed to proceed at 70 °C under inert atmosphere purge for 4 hours (sample GR). Part of this batch was then fully oxidized by bubbling pure oxygen gas through the suspension for 24 hours, washed free of excess salts using high purity water, and reduced again as described above (sample GROR). The level of reduction was measured by digesting a portion of each sample in HF-H_2SO_4 and analyzing the digestate for Fe^{2+} by the method of Komadel and Stucki (1988). Chemical analysis indicated that more than 99% of the octahedral Fe^{3+} was reduced to Fe^{2+}. The total content of Na in GR determined by atomic absorption spectrometry is 3.54 ± 0.20 wt%.

Preparation of films

Highly textured self supporting films of reduced samples were prepared under dry inert atmosphere (N_2 or Ar gas) by filtering the suspensions onto a 0.025 mm pore-size Millipore membrane filter. The resulting oriented clay film was then quickly transferred to a glove box having a H_2O and O2 partial pressure of about 10^{-6} atm. Vibrational modes due to structural O-H stretching and deformation bands were measured in self-supporting clay films containing approximately 2.0 mg of sample per cm^2. Within the glove box, the reduced, dry self-supporting films destined for IR spectroscopy were placed inside a sealed vacuum cell fitted with ZnSe windows (Angell and Schaffer 1965) and pumped to 10^{-6} atm. For P-EXAFS measurements, the mass of clay sedimented onto the Millipore filter was calculated to obtain an absorption jump across the edge ($\Delta\mu$) of typically 0.8 at the experimental α angle of 60° (Stern and Kim 1981). Films were mounted in a vacuum chamber ($P = 10^{-2}$ atm) for polarized X-ray absorption measurements.

Preparation of reference materials

Reference samples for pre-edge spectroscopy include nontronite dehydroxylate, biotite, and FePO4, which were used as standards for $^{V}Fe^{3+}$ (Drits et al. 1995), $^{VI}Fe^{2+}$, and $^{IV}Fe^{3+}$, respectively. The untreated Garfield nontronite film (GO, Manceau et al. 2000) served as a $^{VI}Fe^{3+}$ reference. Nontronite powder was heated to 500 °C for 3 hours to produce the nontronite dehydroxylate, and then stored in sealed tubes filled partially with silica gel desiccant. Powdered mounts of the references were prepared so as to prevent thickness effects on X-ray absorption measurements ($\Delta\mu < 1$, Manceau and Gates 1997; Stern and Kim 1981), and spectra were recorded with the sample rotated at 35° with respect to the electric field vector to eliminate texture effects (Manceau et al. 1990).

X-ray diffraction

Powder X-ray diffraction patterns for GR and GO were recorded on a Siemens D5000 diffractometer equipped with a Si(Li) solid-state detector. Cu*K*α radiation was used with a counting time of 40–50s per 0.04° 2θ step. The GR sample was mounted in a vacuum chamber ($P = 10^{-5}$–10^{-6} atm) to prevent reoxidation.

The intensity distribution and profiles of *hk* bands were calculated using the mathematical formalism of Plançon (1981), Sakharov et al. (1982a, 1982b), and Drits and Tchoubar (1990). Structure factors for GR were calculated from the derived structural formula $Na_{1.30}[Si_{7.22}Al_{0.78}][Fe^{2+}_{3.65}Al_{0.32}Mg_{0.04}]O_{17.93}(OH)_5$ (see "Discussion"). As small variations in the atomic coordinates have no significant influence on the intensity of both the 20–13 and the 13–20 bands (Manceau et al. 2000), the same atomic coordinates were used for both GO and GR samples. Interlayer Na was shifted by 1.05 Å from the middle of the interlayer space toward the nontronite siloxane surface in order to obtain typical distances between interlayer Na and the O atoms defining the hexagonal cavity [d(Na–O) = 2.40–2.50 Å, Bailey 1984]. Unit-cell parameters *a* and *b* = 6*d*(060) and *d*(001) were determined from XRD. Turbostratic layer stacking was simulated by introducing a 100% probability of random stacking faults, and the size and proportion of coherent scattering domains (CSDs) were determined by fitting the 02-11 band profile and assuming that the 003 diffraction line was Lorentzian shaped.

Infrared spectroscopy

Infrared spectra of the structural OH stretching and deformation regions for oxidized (GO) and reduced (GR) Garfield nontronite samples were obtained on self-supporting films oriented perpendicularly to the beam direction. The window material (ZnSe) of the vacuum cell becomes opaque to IR radiation at about 650 cm^{-1}, which overlaps part of the O-H deformation region for the clay samples and therefore defines the lower frequency limit for the analysis. Infrared spectra were collected at a resolution of 0.5 cm^{-1} using a Midac 2000 laser interferometer equipped with a KBr beamsplitter and DTGS (deuterated triglyceride sulfate) detector. Data collection and analysis were performed using the Grams/386 program. The spectrometer was constantly purged by vaporized liquid N_2 to avoid H_2O and CO_2 contamination. To make comparisons among the spectra, holders with a hole of 15 mm diameter were used to mask each film, the peak intensities were normalized to 10 mg/film, and the offset was adjusted for some spectra. No baseline adjustment and curve smoothing were done.

Texture analysis

Quantitative texture analysis (goniometry) was applied to the films following EXAFS measurements using a Huber tex-

ture goniometer in reflectance mode with monochromatized Fe$K\alpha$ radiation point focused to 1 mm. Pole (004) figures were measured in increments of 5° for tilt (ρ) and azimuth (φ) with angular ranges between $0° \le \rho \le 85°$ and $0° \le \varphi \le 360°$. Possible sample inhomogeneities were suppressed with an oscillating sample holder. The method used to normalize the (004) pole figures and express them in distribution densities was detailed in the companion paper (Manceau et al. 2000).

XAS spectroscopy

Polarized (P-EXAFS) and pre-edge spectra were recorded in LURE at Orsay, France, on the D42 station. Data acquisition and reduction were as reported by Manceau et al. (2000). Radial structure functions (RSFs) uncorrected for phase shifts were obtained from the Fourier transform (FT) of k- or k^3-weighted EXAFS spectra ($k\chi$ or $k^3\chi$) to emphasize the contribution from the lower or higher k region, respectively. Interatomic distances (R) and numbers of atomic neighbors (N) for the first three shells (O1, Fe1, Tet1) were determined using experimental phase shift and amplitude functions derived from polarized EXAFS spectra of GO (Manceau et al. 1998). In this mineral Fe is surrounded by six nearest O atoms at an average distance of 2.01 Å, three nearest Fe atoms at $b/3$ = 3.05 Å, and four nearest (Si,Al) atoms at 3.26–3.27 Å. From this reference, uncertainties for R and N of approximately 0.02 Å and 10% for the O1, Fe1, and Tet1 shells can be expected, but the relative accuracy is better. Because of the large reciprocal range explored in this study ($3 \le k \le 14.5$ Å^{-1}), and the very high quality of P-EXAFS spectra, the sensitivity to variations in interatomic distances is as little as 0.01 Å for these three shells. Functions for the long distance (~5 Å) Fe2 shell were calculated ab initio by the FEFF7.02 code (Rehr et al. 1991), and their validity was tested on Garfield nontronite. All reported N values refer to crystallographic values obtained by correcting effective numbers (N_{eff}) from the angular dependence term $<3\cos^2\theta>$ (Manceau et al. 1998). The static disorder in reduced samples is expressed as $\Delta\sigma$, the difference of root-mean-square standard deviations of distances between the reduced samples and the oxidized Garfield reference.

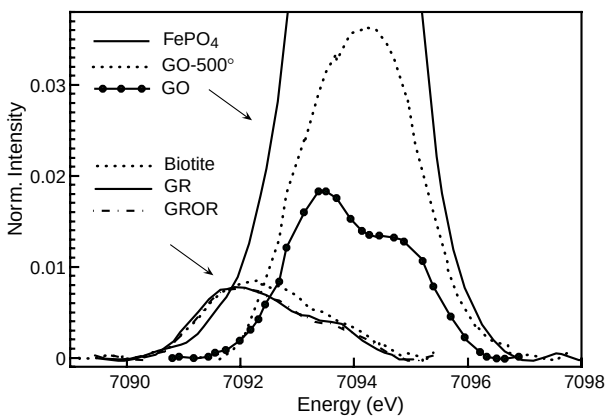

FIGURE 1. Fe K pre-edge spectra for oxidized (GO), reduced (GR) and re-oxidized/re-reduced (GROR) Garfield nontronite, as compared to standards including $^{IV}Fe^{3+}$ (FePO4), 100% $^{V}Fe^{3+}$ (GO-500°), and $^{VI}Fe^{2+}$ (biotite).

RESULTS

Pre-edge spectroscopy

The observed shift in energy (Fig. 1) between the biotite ($^{VI}Fe^{2+}$) and the GO ($^{VI}Fe^{3+}$) references relates to differences in binding energies of the 1s electrons, and to destabilization of antibonding molecular orbitals as the formal valency of the metal ion increases (Manceau and Gates 1997). Additionally, the differences in the spectral intensity between biotite and GO reflects the different degree of filling of the 3d electronic orbitals for Fe^{3+} (d^5) and Fe^{2+} (d^6) ions, because pre-edge spectroscopy directly probes the density of states of 3d-like electronic orbitals.

For a given oxidation state, the pre-edge intensity depends on the symmetry of 3d molecular orbitals, and on the atomic coordination and geometry (Manceau and Gates 1997). It increases from six- to five- to fourfold coordination (Farges et al. 1997). This evolution is apparent in Figure 1 in order of unheated GO ($^{VI}Fe^{3+}$), heated ($^{V}Fe^{3+}$) Garfield and FePO4 ($^{IV}Fe^{3+}$). During heating, phyllosilicates are dehydroxylated (Brindley and LeMaitre 1987; Drits et al. 1995), and the ^{VI}Fe sites of nontronites are transformed to fivefold sites at 500° following the reaction $2OH_{structural} \rightarrow H_2O_{vapor} + O^-_{structural}$. The presence of ^{V}Fe in the nontronite structure decreases the crystal field splitting of the e_g- and t_{2g}-like components of the 3d electronic orbitals (Douglas et al. 1994), which explains the broader shape of heated vs. non-heated samples. Both the GROR and GR pre-edge spectra are similar to that of biotite and are consistent with the presence of structural $^{VI}Fe^{2+}$ (Fig. 1).

Without a suitable reference, we cannot definitively reject the presence of $^{V}Fe^{2+}$ species in the reduced samples. However, one may anticipate from theory, and from results obtained on heated ferric nontronites, that the presence of fivefold Fe^{2+} species would have resulted in a significant increase in the pre-edge Fe^{2+} intensity compared to biotite, and to a decrease of the splitting of 3d orbitals. As will be shown below, the absence of $^{V}Fe^{2+}$ is also supported by the Fe^{2+}-O EXAFS distance.

The strong similarity of the spectra for biotite and the reduced nontronites suggests that essentially all Fe in the structure of GR and GROR is in the reduced state. The maximum amount of unreduced iron was estimated from linear combinations between oxidized Garfield and biotite spectra to be 15% as compared to >99% with the wet-chemical analysis.

X-ray diffraction

Powder XRD patterns of GR and GO (Fig. 2) display only 00l and two-dimensional hk bands typical of a pure turbostratic layered structure (Brindley and Brown 1980). Thus, reduction of Fe^{3+} to Fe^{2+} does not increase noticeably the three-dimensional ordering of nontronite. As expected from the larger size of Fe^{2+} ions, the b unit-cell parameter of GR (9.21 Å) was larger than that of the oxidized sample (9.13 Å). The d(001) distance of the reduced sample (9.732 Å) equals that of GO indicating that all interlayers were collapsed in the dehydrated state. The $I_{02\text{-}11}/I_{20\text{-}13}$ ratio of GR remarkably decreases compared to GO (Fig. 2). The intensity ratio of these two bands depends on the distribution of octahedral cations between M1 and M2 sites within the same octahedral sheet (Drits et al. 1984; Manceau et al. 2000). An

optimum fit was obtained with 28% of total iron ions in M1 sites (Fig. 3a). The M1 site occupancy was varied to estimate the sensitivity of the method for determining the cation distribution over M1 and M2 sites within the same octahdral sheet. Even a small increase of the M1 site occupancy from 28% to 33% of total Fe in M1 sites (Figs. 3a and 3b, respectively) significantly modified the intensity ratio between the 02-11 and the 20-13 bands. All octahedral Al cations are assumed to remain in M2 sites in the GR sample. Fitting of the 20-13 band profile indicated that GR layers have an orthogonal symmetry, with a b/a ratio equal to $\sqrt{3.13}$. The assumption of hexagonal layer symmetry ($b/a = \sqrt{3}$) yielded a poorer fit with the simulated 02-13 band being shifted to higher d values (lower 2θ angle) relative to the experimental band (Fig. 3c).

Three disk-shaped CSDs were necessary to reproduce the profile of the 02-11 band. They had radii of 200 Å, 100 Å, and 60 Å and their relative abundance was 1:5:6, respectively. In GO, two CSDs of 200 Å and 100 Å radii and relative abundance of 1:1.2 were sufficient to fit the profile (Manceau et al. 2000). Consequently, the reduction of nontronite results in a significant decrease of CSD diameters. This decrease of the structural order within the layer plane can be observed in Figure 3d which compares the experimental pattern for GR to the optimal simulation obtained for GO: the 02-11 band is clearly broadened in the reduced state. Finally, XRD results indicate that 28% ± 5% of octahedral Fe cations, initially entirely present only in M2 sites of the untreated GO nontronite, are present in M1 sites. The presence of occupied M1 (trans) sites implies that Fe ions migrated from M2 to M1 sites in the nontronite structure due to the reduction of Fe^{3+} to Fe^{2+}.

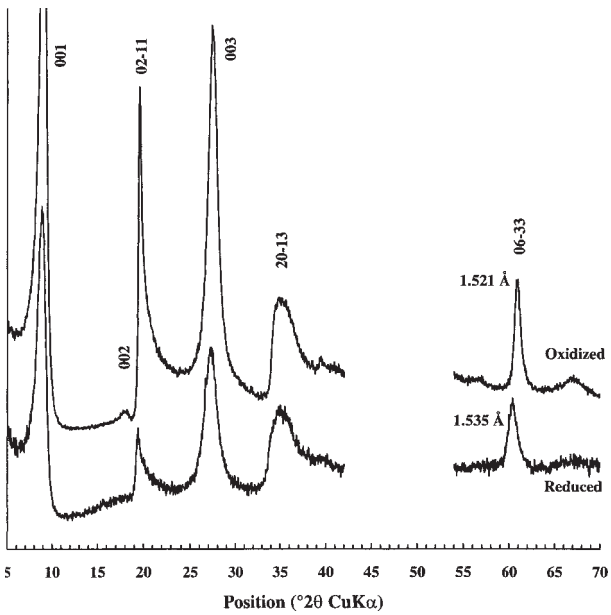

FIGURE 2. Experimental powder X-ray diffraction patterns for the oxidized (GO, above) and reduced (GR, below) Garfield nontronite samples. Diffraction maxima are indexed, and $d(060)$ is indicated for each sample.

IR spectroscopy

O-H stretching region. For the oxidized mineral, the structural O-H absorption band was relatively sharp and centered near 3570 cm^{-1} (Fig. 4a). This position is typical for OH coordinated predominantly with two Fe atoms ($[Fe^{3+}]_2$) in the octahederal sheet of dioctahedral smectites (Russell et al. 1979) and is rather symmetrical, indicating a high Fe^{3+} content. Notice the very low absorbance of H_2O stretching bands between 3000 and 3500 cm^{-1}, confirming that the method for minimizing interference due to adsorbed water was successful.

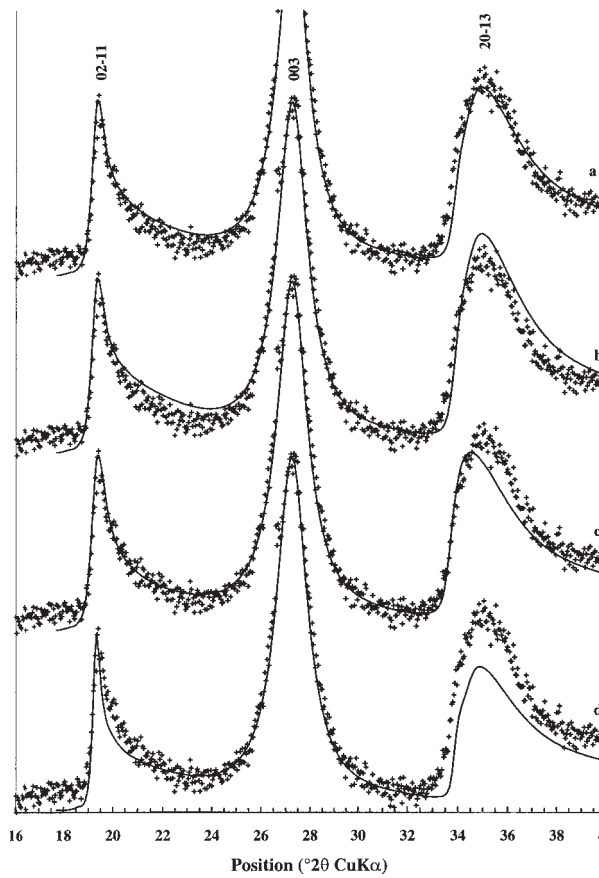

FIGURE 3. Comparison between experimental and calculated XRD patterns. (**a**) Optimum fit obtained for reduced Garfield nontronite (GR) assuming 28% of total iron in trans sites and 72% in cis sites. All aluminum cations are supposed to remain in cis sites. (**b**) XRD pattern calculated for GR with 33% of total iron occupying trans sites. (**c**) XRD pattern calculated for GR assuming an hexagonal layer symmetry with $a = b\sqrt{3} = 5.317$ Å instead of 5.21 Å in the optimum case. (**d**) XRD pattern calculated for GR sample by using a 5:6:0 ratio, as for GO sample, between CSDs having 200 Å, 100 Å, and 60 Å radii, respectively. Experimental profiles are shown as crosses, and the calculated patterns are plotted as solid lines. All calculations were perfomed by using the chemical composition derived from the proposed model, and atomic coordinates from Manceau et al. (2000). For all calculations $a = 5.21$ Å, $b = 9.21$ Å, and $d(001) = 9.732$ Å. Except for Figure 3d, a 1:5:6 ratio between CSDs having 200 Å, 100 Å, and 60 Å radii, respectively, was used.

Reduction of structural Fe changed the entire absorption envelope (Fig. 4a). The OH signature is now a broad located at about 3530 cm^{-1} on a more prominent band centered near 3370 cm^{-1}. We tentatively attribute the latter band to strongly absorbed or bound H_2O that survived dehydration. The change in position and intensity of the primary structural OH cationic band suggests a major rearrangement in the OH environment after reduction. Further evidence confirming this is the appearance of a sharp peak at 3623 cm^{-1} (spectrum B), because this position is uncharacteristic for OH surrounded by ferric Fe in dioctahedral phyllosilicates (Besson and Drits 1997; Slonimskaya et al. 1986). Burns and Strens (1966) reported the existence of fundamental O-H stretching vibrations of $[Fe^{2+}]_3OH$ at 3625 cm^{-1} and 3615 cm^{-1} in two amphibole series (tremolite-ferroactinolite and cummingtonite-grunerite). In biotite the center of the complex OH stretching band appears near 3620 cm^{-1} (Barshad and Kishk 1968). Based on the XRD evidence for 28% trans-site occupancy in the reduced nontronite, we propose that the absorption band at 3623 cm^{-1} is attributed to $[Fe^{2+}]_3OH$ domains of trioctahedral character. The band near 3623 cm^{-1} reveals that reprotonation occurred after formation of the trioctahedral character.

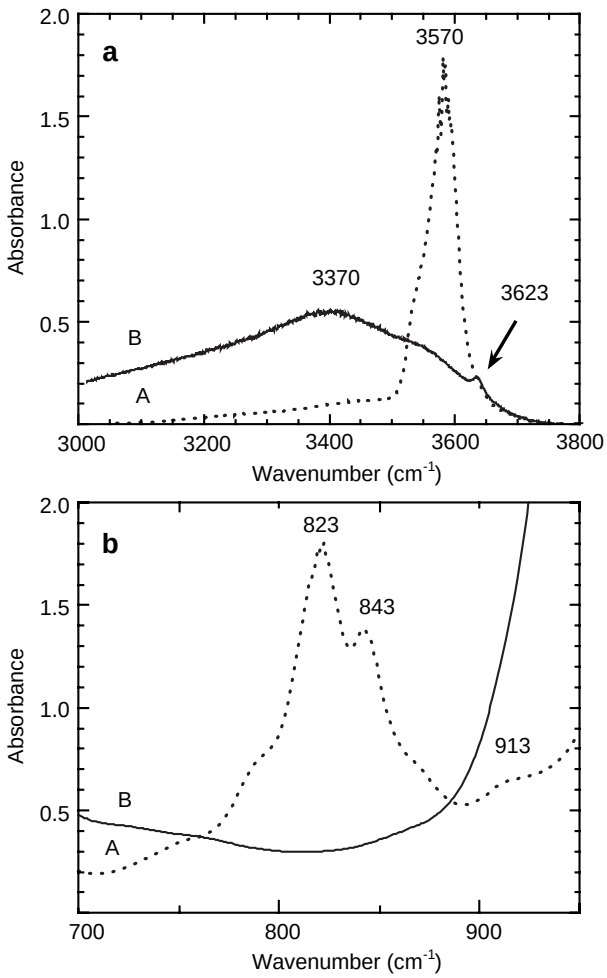

FIGURE 4. Infrared spectra of oxidized (A) and reduced (B, 4 h at 70° with dithionite) Garfield nontronite. (**a**) structural hydroxyl stretching region; (**b**) structural M-O-H deformation region.

M-O-H deformation region. The oxidized Garfield (spectrum A, Figure 4b) has the classic peak at 823 cm^{-1}, assigned to $[Fe^{3+}]_2OH$ deformation. Less certain is the interpretation of the peak at 843 cm^{-1}. Goodman et al. (1976) assigned it to either $AlFe^{3+}OH$ or OH librations associated with trans Fe. Stucki and Roth (1976) found that the shift in this peak upon deuteration corresponds closely to that expected if the oscillators had the masses of reduced Fe and OH/OD, but the same effect would be observed if the bending vibration is highly constrained. However, in spite of the uncertain assignment of these bands, they together are typical for, and even diagnostic of, nontronites (Russell et al. 1979; Farmer, 1974).

Upon Fe reduction the 950–700 cm^{-1} region became virtually featureless, with both $[Fe^{3+}]_2OH$ librations disappearing, and thus presenting further strong evidence for the absence of dioctahedral character in the reduced smectite. Huo (1997) reported that the disappearance of the $[Fe^{3+}]_2OH$ bands in reduced nontronites was accompanied by the growth of a new peak at 656 cm^{-1}, which is near the region where $[Fe^{2+}]_3OH$ deformation modes are expected (Wilkins and Ito 1967), thus further supporting the formation of trioctahedral Fe^{2+} domains as demonstrated by XRD.

Film characterization by texture analysis

From pole figures, the maximum density of orientation equals 10.6 mrd for GR and 13.6 mrd for GROR (Fig. 5). These are less than the value of 37.1 mrd obtained for the oxidized sample (GO) but similar to that of 14.3 mrd for the Washington nontronite SWa-1 (Manceau et al. 2000). The two reduced samples have a FWHM of 44.9° (GR) and 38.8° (GROR) as compared to 19.6° for GO and 38.2° for SWa-1. Thus, the dispersion from perfect alignment of particles in the film plane of the reduced samples is almost identical to that obtained for SWa-1. Manceau et al. (1998, 1999) showed that the difference between N_{eff}, estimated from the crystallographic structure assuming an idealized texture, and the value measured by P-EXAFS (N_{exafs}) is equal to 11% at $\alpha = 90°$ for the Oct-Tet1 pair, and to 4% at $\alpha = 0°$ for the Oct-Oct1 pair assuming a continuous inclination of ±20° of the c^* axis symmetrically around the film normal. Consequently, the dispersion of crystallites in GR and GROR ($\Delta\rho \approx \pm 20°$) remains fairly acceptable and should only marginally affect N_{eff} values.

P-EXAFS spectroscopy

Angular dependence of EXAFS spectra and RSFs. The variation of the EXAFS spectra (Fig. 6) as a function of experimental angle (α) is pronounced in the 2.5–10 $Å^{-1}$ range, confirming the successful preparation of highly oriented films in the reduced state, just as was obtained for the oxidized samples (Manceau et al. 2000). However, a marked difference from the EXAFS spectra of oxidized Garfield (see Fig. 7 in Manceau et al. 2000) is the loss in amplitude of $k^3\chi(k)$ above 10 $Å^{-1}$, reflecting a decreased short-range order in reduced nontronites. Due to this loss in spectral amplitude, the angular variation of the amplitude is diminished and becomes progressively smeared out in the noise.

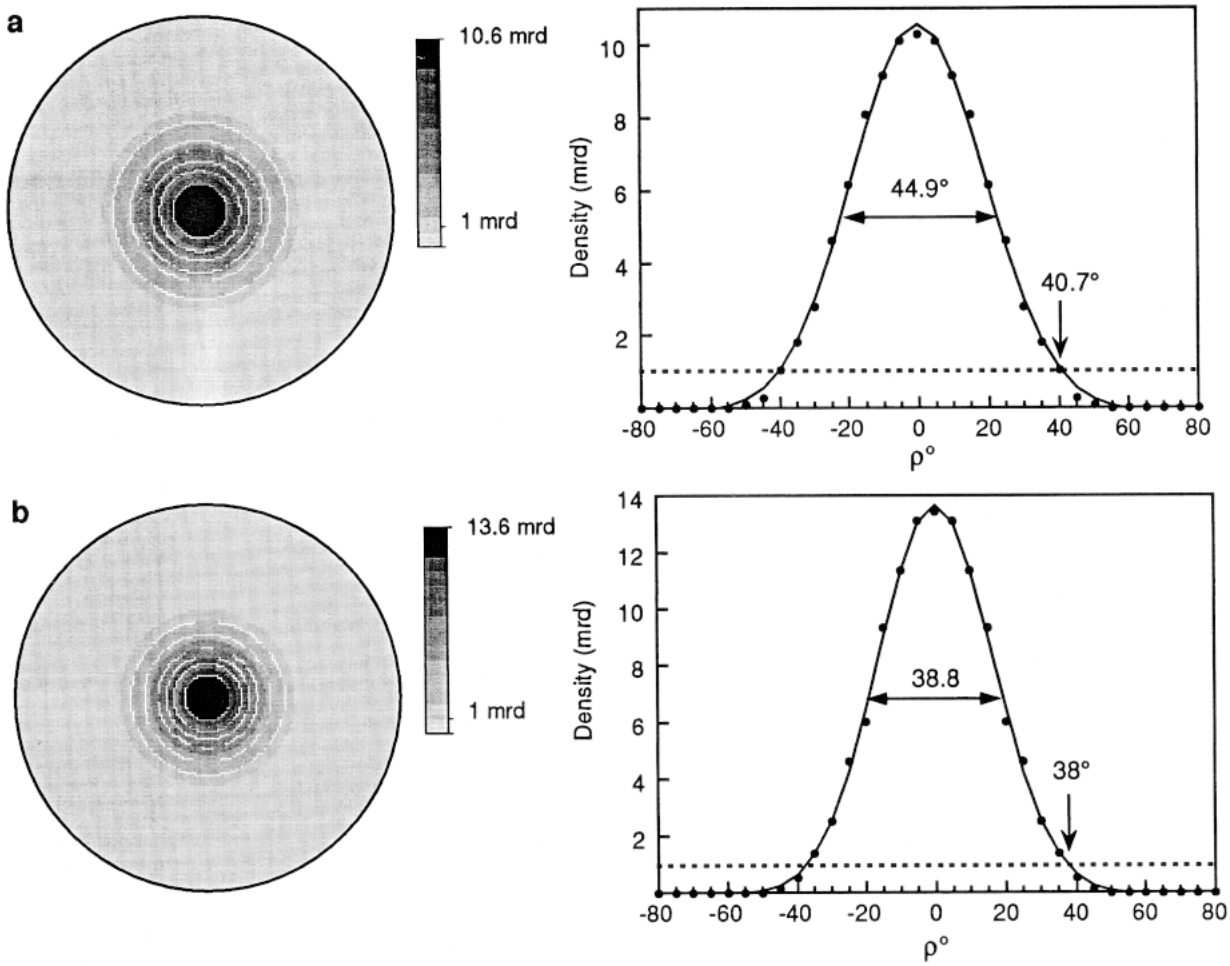

FIGURE 5. Pole figures for the 004 reflection (**left**) and corresponding radial distribution densities (**right**) for GR (**a**) and GROR (**b**). The distribution maxima are for the centre of the pole figures ($\rho = 0°$). The 1 mrd level (perfectly random powder) is indicated by a dashed line. Linear density scales and equal area projections are used for the pole figures.

The out-of-plane ($\alpha = 90°$) spectra (Fig. 6) were calculated using a linear regression method described elsewhere (Manceau et al. 1988, 1998). The quality of this linearization can be assessed visually by overplotting experimental and recalculated EXAFS spectra at any particular experimental angle ($0° \leq \alpha \leq 60°$), and statistically by calculating profile reliability factors (R_p, Table 1) between experimental and recalculated spectra. This analysis (Figs. 7a and 7b; Table 1), shows that the experimental $k^3\chi(\alpha = 0°)$ spectrum for GR is indistinguishable from that recalculated from regression. The mean value of R_p ($<R_p>$) averaged over the 5 experimental angles was 1.9×10^{-3} (GR) and 1.3×10^{-3} (GROR). These fairly low values are similar to that obtained for the oxidized sample (0.8×10^{-3}), and provide confidence for the calculation of $k^3\chi(\alpha = 90°)$ theoretical spectra. R_p values (Table 1) also give an estimate of the precision for the measurement of EXAFS spectra.

The experimental $k^3\chi(\alpha = 0°)$ and recalculated $k^3\chi(\alpha = 90°)$ spectra GR and GROR (Figs. 7c and 7d) bear strong resemblance at both $\alpha = 0°$ and $\alpha = 90°$, which indicates that the two reduced samples possess essentially the same in-plane and out-of-plane structures. Several oscillations of GROR have a slightly higher amplitude than GR, suggesting that the two samples have a slightly different structural order. Note that this difference of spectral amplitude between GR and GROR can not be interpreted by a difference of texture strength because GROR, which has the highest texture, would have a larger angular dependence and, consequently, a higher spectral amplitude at $\alpha = 0°$ and a lower amplitude at $\alpha = 90°$ than GR. The oscillations peaking at $k = 6$ and 6.5 $Å^{-1}$ (Figs. 7c and 7d) show that GROR has instead a higher spectral amplitude for the two angles. Apart from this small difference, interpreted below, the two samples obviously have a similar structure, and for this reason we focus on GR.

The comparison of oxidized (GO) and reduced (GR/GROR) P-EXAFS spectra is also insightful. EXAFS spectra have a higher frequency in the reduced than in the oxidized state regardless of the orientation angle. This phase shift reflects a difference in Fe-O and Fe-Fe distances caused by the larger size of Fe^{2+} compared to Fe^{3+}. If one excludes this difference of wave phase, the $k^3\chi(\alpha = 90°)$ spectra (Fig. 7d) of the oxidized

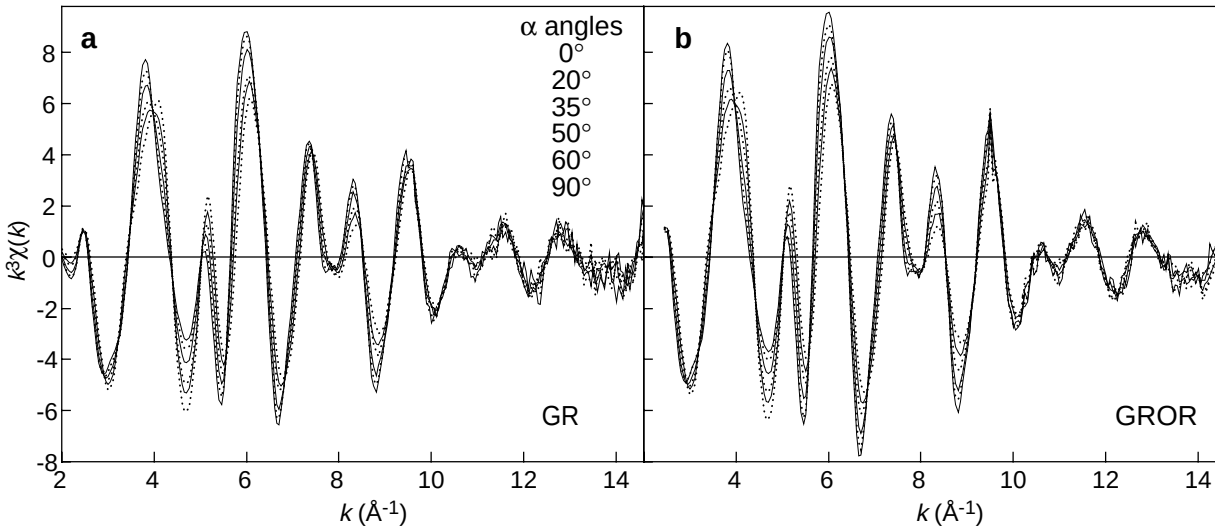

FIGURE 6. k^3-weighted Fe K-edge P-EXAFS spectra for GR (**a**) and GROR (**b**) at α angles of 0°, 20°, 35°, 50°, 60°, and 90°, where α is the angle between the electric field vector and the film plane. The 90° spectrum has been obtained by regression of the experimental amplitudes for $0° \le \alpha \le 60°$. The amplitude of χ decreases with increasing α at 6.0 Å^{-1}, and increases with α at 5 Å^{-1}. Note the presence of isosbestic points where $\chi(k,\alpha)$ is independent of k.

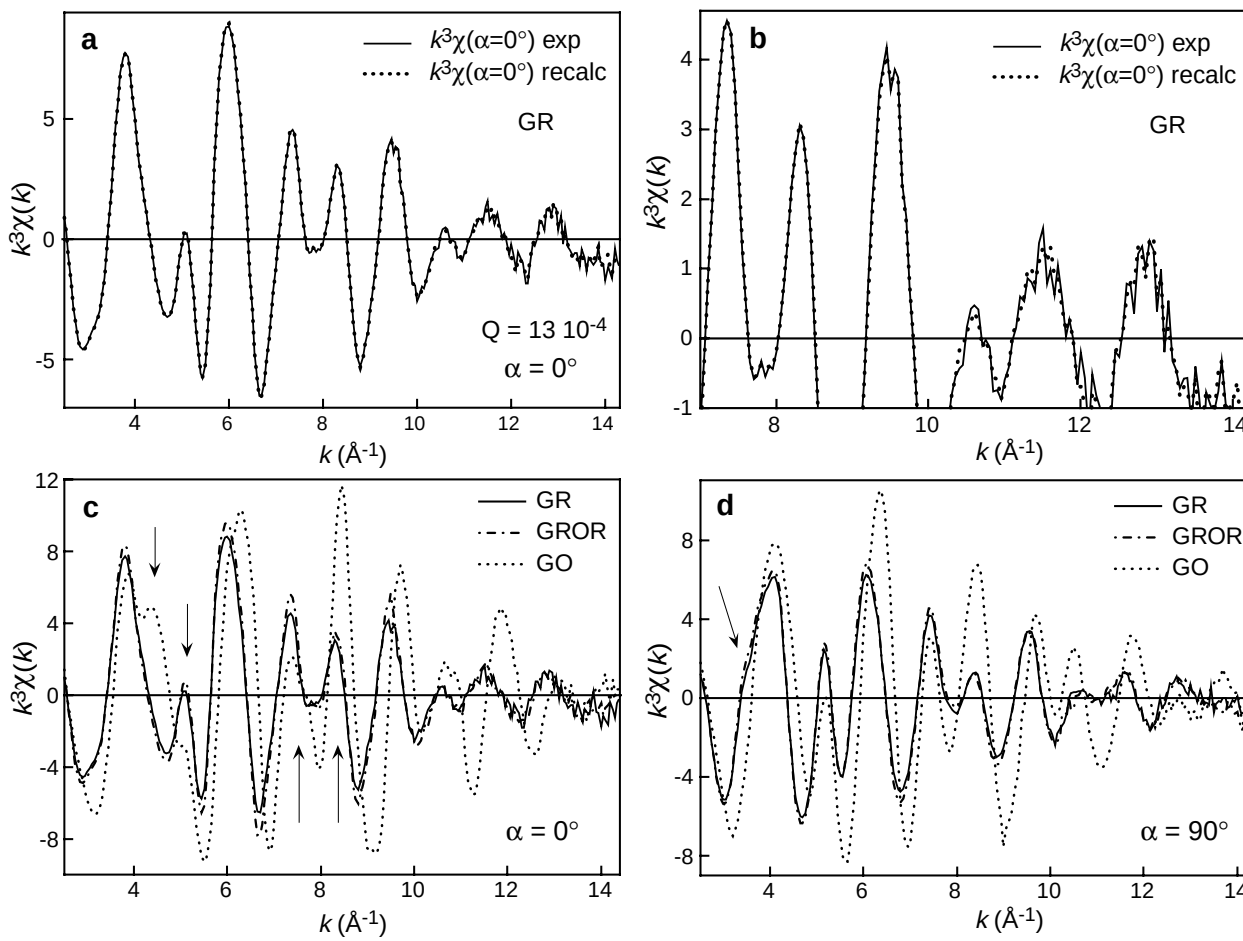

FIGURE 7. (**a**) Experimental and recalculated $k^3\chi$ (α = 0°) functions for GR. (**b**) Zoom of (**a**). (**c**) Comparison of experimental $k^3\chi$ (α = 0°) functions for GR, GROR, and GO. (**d**) Comparison of experimental $k^3\chi$ (α = 90°) functions for GR, GROR, and GO.

TABLE 1. Profile reliability factor (R_p) between experimental and recalculated P-EXAFS spectra

	α = 0°	α = 20°	α = 35°	α = 50°	α = 60°	< R_p >
GO	$8\ 10^{-4}$	$9\ 10^{-4}$	$9\ 10^{-4}$	$6\ 10^{-4}$	$6\ 10^{-4}$	$8\ 10^{-4}$
GR	$1.3\ 10^{-3}$	$2.4\ 10^{-3}$	$2.7\ 10^{-3}$	$1.9\ 10^{-3}$	$1.0\ 10^{-3}$	$1.9\ 10^{-3}$
GROR	$1.1\ 10^{-3}$	$1.8\ 10^{-3}$	$2.0\ 10^{-3}$	$1.0\ 10^{-3}$	$8\ 10^{-4}$	$1.3\ 10^{-3}$

Notes: R_p is the figure of merit for the spectral fitting, $R_p = \Sigma\ (k^3\chi_{exp} - k^3\chi_{th})^2 / \Sigma\ (k^3\chi_{exp})^2$.

and reduced nontronite have a similar shape, whereas $k^3\chi(\alpha = 0°)$ spectra (Fig. 7c) do not. The only substantial difference in the $k^3\chi(\alpha = 90°)$ spectra is the appearance of a shoulder at 3.4 Å^{-1} (arrow in Fig. 7d), indicating that less severe structural modifications may be expected in the tetrahedral than in the octahedral sheets of reduced nontronite. In $k^3\chi(\alpha = 0°)$ for GR and GROR the wave maximum at 4.4 Å^{-1} is lost whereas the maximum at 5.10 Å^{-1} is amplified (see arrows), and the relative intensity of the two maxima at 7.4 Å^{-1} and 8.4 Å^{-1} is reversed in the two oxidation states. Lastly, the loss in amplitude of $k^3\chi(k)$ with increasing k noted previously in Figure 6 is more marked in the in-plane than in the out-of-plane orientation when we compare oxidized and reduced samples. This observation suggests that the source of disorder originates from distant Fe-Fe pairs because the high k range is dominated by the contribution of Fe atoms (see Fig. 2 in Manceau et al. 2000). All spectral modifications noted in the parallel orientation indicate that the reduction of Fe impacts the structure of the octahedral sheet of nontronite and, specifically, the coherency of Fe-Fe interactions.

Six peaks are seen in the RSFs corresponding to k- and k^3-EXAFS spectra for GR (Fig. 8) (also referred to as FT[$k\chi$] and FT[$k^3\chi$]). Peak A can be assigned to the nearest oxygen shell (O1) ; peak B results from the combined effect of the nearest Fe, the nearest (Si,Al = Tet1) and the next-nearest oxygen shells (Fe1 + Tet1 + O2); peak D is assigned to the next-nearest (Si,Al) shell (Tet2); and peak E to the next-nearest Fe shell (Fe2) (Manceau et al. 1998; see Fig. 11 in Manceau et al. 2000). The polarization dependence of each peak is similar to that found in GO (Manceau et al. 1998), and conforms to the structure of a phyllosilicate. Two additional peaks, C and F, are not observed in oxidized Garfield. The former has a maximum intensity at α = 90°, and the second at α = 0°. These two peaks deserve special consideration and they will be analyzed below, following the analysis of the O1 shell.

First oxygen shell analysis. The first oxygen shell contribution of GR (Peak A) is much lower in amplitude than that of GO (see Fig. 11a in Manceau et al. 2000). In the oxidized state the amplitude of peak A is 340 (arbitrary unit) compared to 200 in the reduced state. This amplitude reduction is not associated with a loss of oxygen nearest neighbors because preedge spectroscopy indicates that Fe^{2+} is located in sites coordinated by six O atoms. Instead, the decrease in amplitude suggests that average Fe^{2+}-O distances in reduced nontronite are more incoherent than average Fe^{3+}-O distances in oxidized nontronite.

To estimate the changes in the Fe-O distances with reduction, peak A for GR was Fourier back-transformed in the [1.2–2.2] Å range and, by least-squares procedures, the average Fe^{2+}-O distance and the number of O atoms coordinated to Fe^{2+}

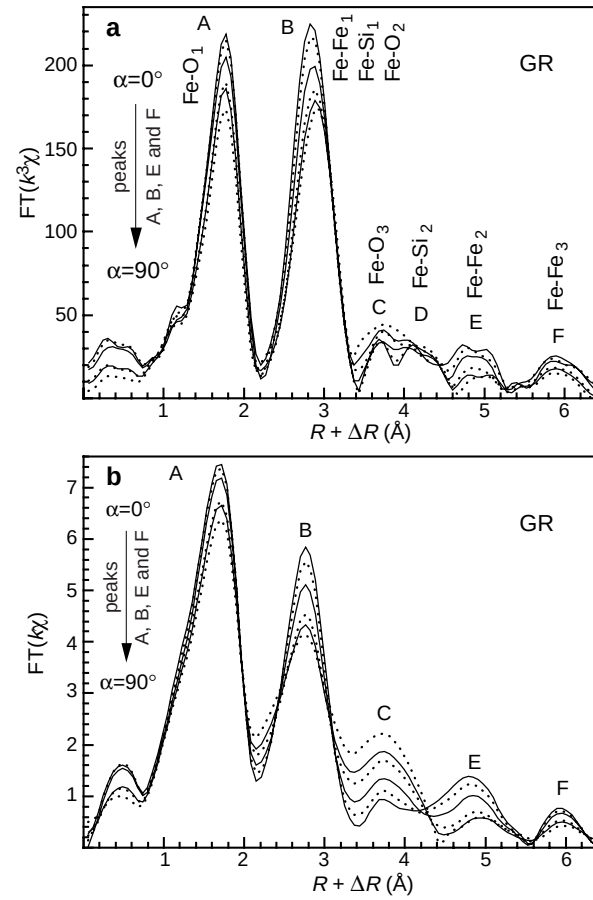

FIGURE 8. k^3-weighted (**a**) and k-weighted (**b**) Fe K-edge polarized RSFs for GR at α angles of 0°, 20°, 35°, 50°, 60°, and 90°. The amplitude of peaks A, B, E, and F decreases with increasing α.

were determined. The precision of N and R was estimated by altering the spectral adjustment by 2 R_p. The best spectral fit ($R_p = 4 \times 10^{-3}$) was obtained by assuming 5.3 ± 0.8 O atoms at 2.10 ± 0.01 Å ($\Delta\sigma$ = 0.02 Å) (Fig. 9a). A Fe-O bond length of 2.10 Å is characteristic of $^{VI}Fe^{2+}$ species. Both the 0.02 Å increase in the differential disorder term ($\Delta\sigma$), and the decrease of N_O from 6.0 to 5.3, relative to GO, are significant and originate from the greater spread in the average Fe-O bond distance in the reduced state. Because N and σ are interdependent (Teo 1986), the incoherency of Fe-O distances and the apparent loss of O neighbors can both be accounted for by a simultaneous increase in $\Delta\sigma$ and a decrease in N_O. The maximum amount of unreduced $^{VI}Fe^{3+}$ in GR was estimated by performing two-shell fits with differing N_O values for the sub-shells at 2.01 Å (Fe^{3+}-O) and 2.10 Å (Fe^{2+}-O) , while fixing the other parameters to their value in the reference ($\Delta E = \Delta\sigma = 0.0$). The addition of 7% $^{VI}Fe^{3+}$ (N_O = 0.4) resulted in a doubling of R_p (Fig. 9b), and indicates that introducing a small amount of Fe^{3+} alters the match between the two phases in the 9 Å^{-1} < k < 13 Å^{-1} interval, as well as affects the amplitude envelopes. We can conclude from

this analysis that Fe^{2+} represents at least 93% of the total Fe in the reduced Garfield sample, which is in agreement with pre-edge and chemical analysis results.

Analysis of out-of-plane contributions. Application of P-EXAFS to layer silicates is a powerful technique which allows the isolation and subtraction of the minor tetrahedral sheet contribution from the predominant octahedral sheet contribution (Manceau et al. 1998; 1999). Certain spectral features originating from the tetrahedral sheet provide structural information. Comparison of FT[$k^3\chi(\alpha = 90°)$] and FT[$k\chi(\alpha = 90°)$] functions shows that the Fe-Tet1 contribution (peak B) has a lower amplitude in the reduced sample (Figs. 10a and 10b). The loss in amplitude may originate either from a decrease in the number of Fe-Tet1 pairs (for example, as a consequence of migration of Fe^{2+} out of the clay structure) or from a wider distribution of the Fe-(Si,Al) distances. Determination of which factor is responsible can be achieved by comparing calculated and experimental envelopes of the Fourier filtered EXAFS contributions [$\chi_{Tet1}(\alpha=90°)$]. As a result of structural loss of Si,Al nearest neighbors (first possibility), the wave amplitude will decrease, but its shape will be preserved [$A_{Si}(k)$ function]. On the contrary, a wider distribution of the Fe-Tet1 distances (second possibility) increases the wave damping, or signal loss, in k space (i.e., increase of σ). Figure 11a shows that the second interpretation is the more appropriate explanation for the loss in amplitude of the Fe-Tet1 contribution (peak B, Fig. 10) because the $k^3\chi_{Tet1}(\alpha = 90°)$ spectra for GO and GR have similar amplitudes near 4 Å^{-1} but not at greater k and the relative difference in amplitude increases progressively from ~5 Å^{-1} to ~11 Å^{-1}. Also, GR has a slightly higher wave frequency, indicating that the Fe-Tet1 distances are larger in the reduced state. Assuming a single Fe-Tet1 distance provided an approximate fit to this spectrum (R_p = 0.027, Fig. 11b). However, the phase mismatch at higher k values suggested the presence of at least two discreet Fe-Tet1 distances. Thus, a two-shell fit to $k^3\chi_{Tet1}(\alpha$

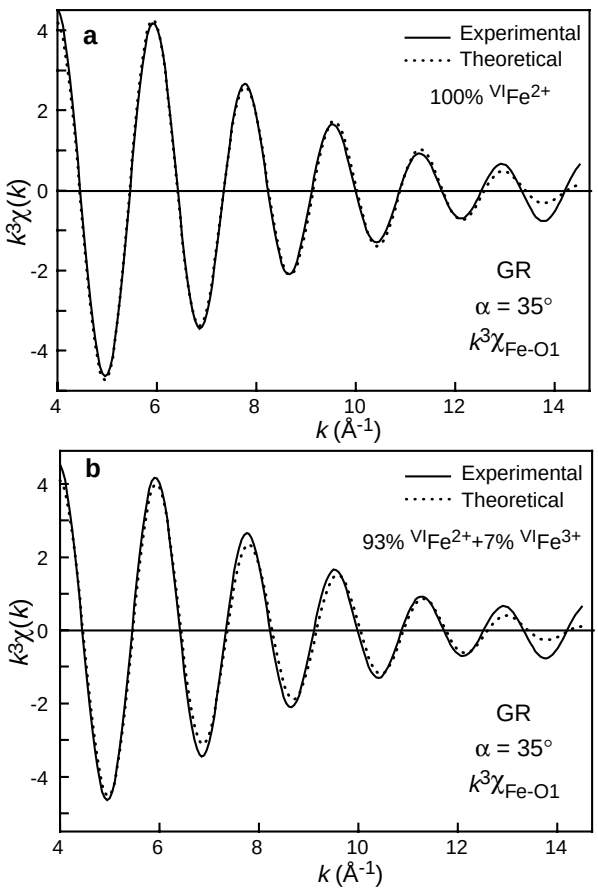

FIGURE 9. Fourier-filtered $k^3\chi_{Fe\text{-}O1}(\alpha = 35°)$ contribution to EXAFS spectrum of GR. (**a**) Best spectral fit ($R_p = 4 \times 10^{-3}$) obtained by assuming 5.3 ± 0.8 O atoms at 2.10 ± 0.01 Å ($\Delta\sigma$ = 0.02 Å). (**b**) Spectral simulation assuming a mixture of 7% $^{VI}Fe^{3+}$ and 93% $^{VI}Fe^{2+}$.

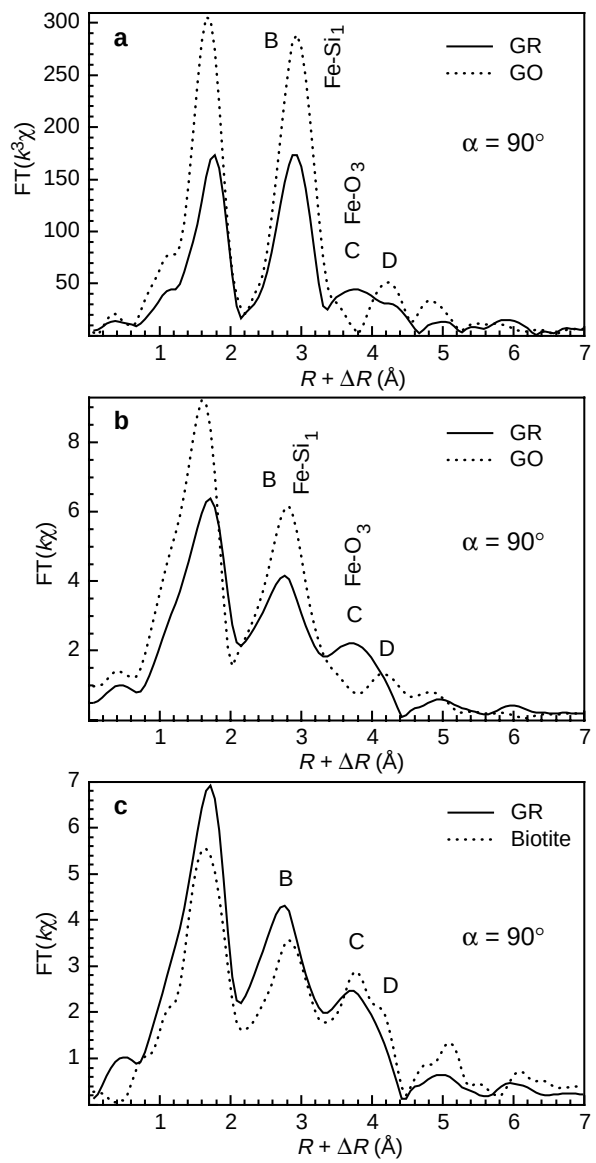

FIGURE 10. RSFs functions in the normal orientation. (**a**) k^3-weighted RSFs for GR and GO. (**b**) k-weighted RSFs for GR and GO. (c) k-weighted RSFs for GR and a trioctahedral biotite sample.

= 90°), assuming R_{Tet1} = 3.28 Å, N_{Tet1} = 3.1 ± 0.5 (Δσ = 0.00 Å) and R_{Tet1} = 3.44 Å, N_{Tet1} = 0.9 ± 0.4 (Δσ = 0.00 Å) yielded better agreement over the entire *k* range (R_p = 0.002, Fig. 11c). The precision on *N* was estimated from a 2 R_p variation of the fit quality.

Peak C is absent in GO (Fig. 10), but is present in the reduced samples. Comparison of the FT[$k^3\chi(\alpha = 90°)$] (Fig. 10a) and FT[$k\chi$ (α = 90°)] (Fig. 10b) RSFs functions shows that the amplitude of peak C is increased by *k*-weighting relative to peaks B (Fe-Tet1) and D (Fe-Tet2), which indicates that it is

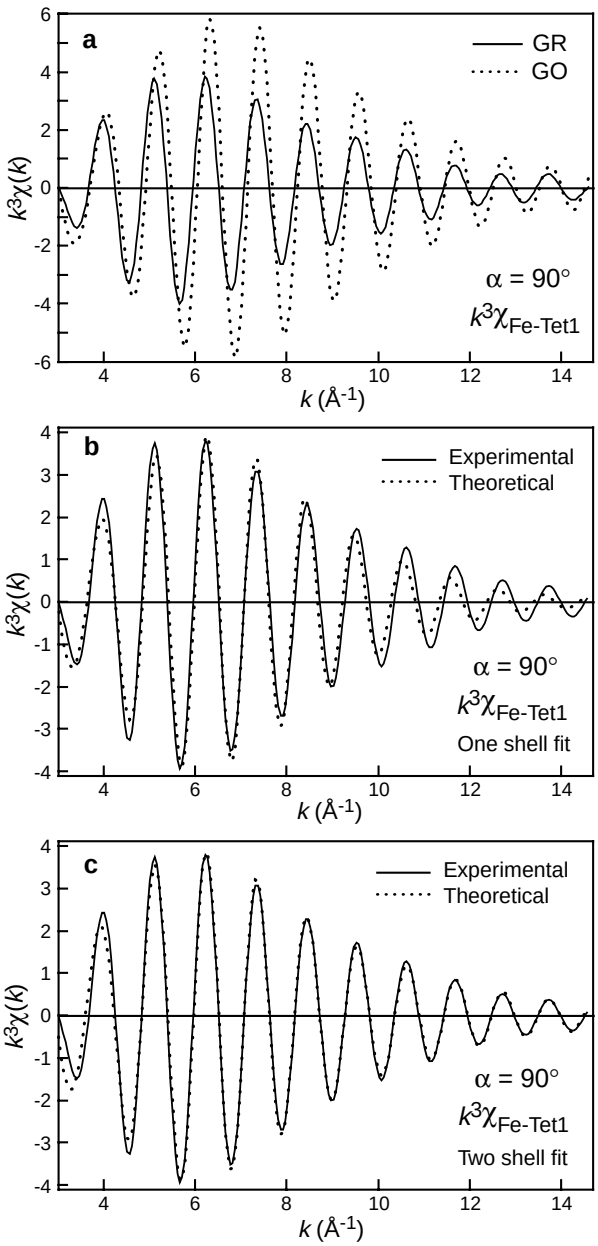

FIGURE 11. Fourier-filtered $k^3\chi_{Fe\text{-}Tet1}(\alpha = 90°)$ contributions to EXAFS spectra. (**a**) Comparison of partial EXAFS spectra for GR and GO. (**b**) One shell fit for GR. (**c**) Best two-shell spectral fit for GR.

associated with out-of-plane oxygen atoms (Manceau et al. 2000). Manceau et al. (1998) showed by *ab initio* FEFF calculations that this O3 atomic shell is located on the basal planes of clay layers (see Fig. 1b in Manceau et al. 2000). Peak C is absent in dioctahedral clay structures, because of corrugation of the basal oxygen plane (Lee and Guggenheim 1981), which increases the average spread in the four Fe-O3 distances. Trioctahedral structures generally have a less corrugated oxygen basal plane and, consequently, less difference is found in the distances of the four third-nearest O3 atoms from the central Fe atom. In the trioctahedral phyllosilicate biotite, this O3 shell is inclined by ~37° off *c** (Takeda and Ross 1975), thus its contribution is greatly enhanced in the perpendicular orientation. This effect is displayed in Figure 10c, a comparison of the RSFs for GR and biotite (no. B13 in Manceau et al. 1990). The similarity of the two FT[$k\chi$ (α = 90°] functions in the 3.4 Å < $R + \Delta R$ < 4.5 Å interval is remarkable, and constitutes a strong argument in favor of the formation of trioctahedral Fe^{2+} clusters in the octahedral sheet of reduced Garfield as implied by XRD and IR analyses.

Analysis of in-plane contributions

Assignment of RSFs peaks. The in-plane orientation (Fig. 12) amplified the contributions from successive Fe shells. In addition to the prominent Fe-Fe contributions, O3 (peak C), and Tet2 (peak D) shells from the tetrahedral sheet are still detected, because these pairs are not orthogonal to the *ab* plane (Fig. 1b in Manceau et al. 2000). The O2 shell (B1) is detected to the right of the Fe-Fe1 (B) contribution in GO when the Fourier transform is performed on *k*c (Fig. 12b), but not in GR. In the reduced state Fe^{2+}-Fe^{2+}1 (B) and Fe^{2+}-O2 (B1) contributions overlap for steric reasons, and are too close to separate by Fourier transform.

Up to three Fe-Fe contributions (B, E, and F in Fig. 12) can be identified in the RSF for GR. Successive Fe shells are represented in Figure 13 by circles of radius *R*. Peak B, at an apparent (uncorrected for phase shift) distance of $R_{Fe1} + \Delta R$ = 2.8 Å, and peak E, at $R_{Fe2} + \Delta R$ = 5 Å, correspond to the nearest Fe1 shell at $R_{Fe1} \approx b/3$ = 3.07 Å, and to the next-nearest Fe2 shell at $R_{Fe2} \approx a = b/\sqrt{3}$ = 5.32 Å, respectively, as for GO (Manceau et al. 1998). In GR peak F is at $R + \Delta R$ = 5.9 Å, so that $R \sim 2R_{Fe1}$. This simple analysis indicates that peak F corresponds to a third Fe shell at $R \approx$ 6.14 Å.

The Fe3 shell contribution is more intense in trioctahedral layer structures (Fig. 12c) owing to the increased alignment along [010], [310] and [$\bar{3}$10] of Fe, Fe1, and Fe3 atoms, which amplifies multiple scattering (MS) paths of the photoelectron (Fig. 13a) (Manceau et al. 1998). This focusing effect is commonly observed in layered metal oxides and hydroxides (O'Day et al. 1994), and occurs when atoms are aligned with little variation in the cation-cation distances. In trioctahedral clay structures all the odd shells (Fe1, Fe3, Fe5…) are aligned along [010], [310], and [$\bar{3}$10] with a periodicity of *b*/3 = 3.05–3.10 Å, and, as such, their contribution is systematically reinforced. This contrast with even shells, which are aligned along [100], [110], and [1$\bar{1}$0], and are separated by much longer distances, approximately a = 5.32 Å. The Fe6 shell is thus too far (~10.6 Å) to be detected. The Fe4 shell is at shorter distance (~8.12

Å) than Fe6, and might be detected, but does not occupy a focussing position as there is no Fe atom located between Fe4 and the central Fe scatterer. Consequently, Fe2 is the only even shell detected in the RSF of phyllosilicates (peak E, Fig. 12). In dioctahedral structures such as GO, the Fe3 shell (peak F) is not detected because at the Fe1 radial position along the Fe-Fe1-Fe3 MS path no atom is present (Fig. 13b) (Manceau et al. 1998).

The assignment of peak F to a Fe shell is confirmed by inverse Fourier transform analysis (see below). The appearance of this Fe3 contribution, and the persistence of the Fe2 contribution after reduction of structural Fe^{3+} provides evidence for the formation of trioctahedral Fe^{2+} domains within the octahedral layers of reduced nontronite. This result is consistent with the analysis of the out-of-plane structure (cf. previous section), from which this structural transformation was inferred from the loss of corrugation of the oxygen basal plane through the appearance of the basal plane Fe-O3 contribution (Fig. 10). The analysis of Fe-Fe contributions at the in-plane orientation also offers a clue for understanding the structural mechanism

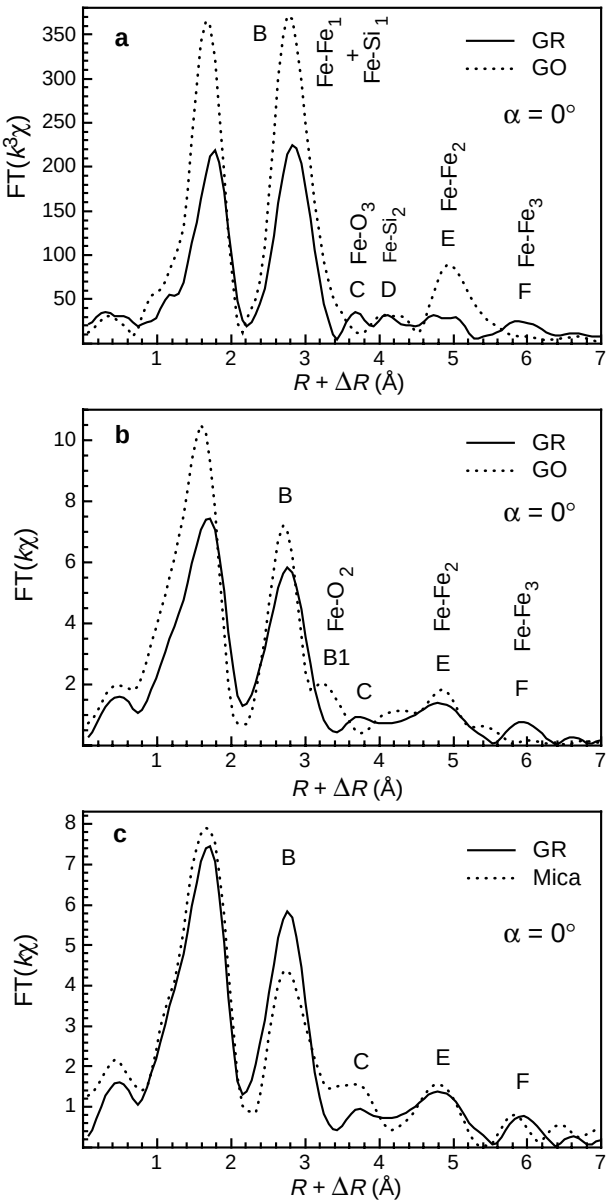

FIGURE 12. RSFs functions in the parallel orientation. (**a**) k^3-weighted RSFs for GR and GO. (**b**) k-weighted RSFs for GR and GO. (**c**) k-weighted RSFs for GR and a trioctahedral biotite sample.

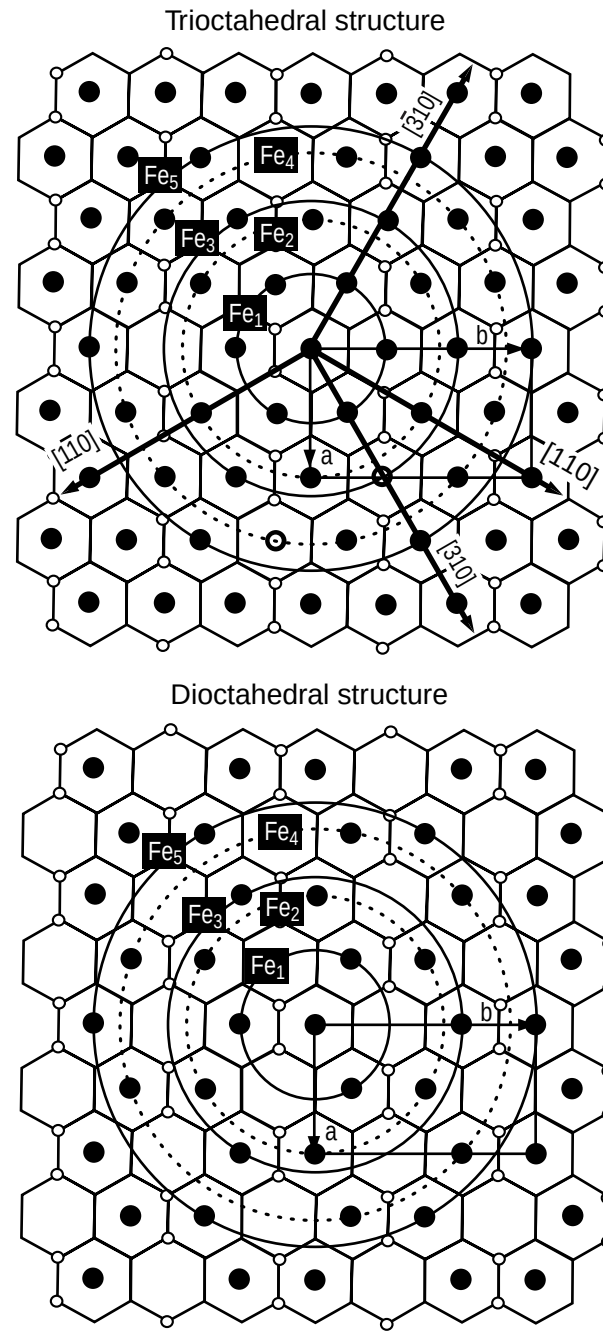

FIGURE 13. Representation of the successive Fe shells in the octahedral sheet of a trioctahedral (**a**) and a dioctahedral (**b**) layer silicate.

of the reduction process in nontronite.

Given the structural importance of the modification observed in the in-plane RSF, whether or not the Fe3 shell can be detected on raw EXAFS spectra would be of interest to assess its reliability. This analysis was performed by comparing the full experimental EXAFS spectrum for GR to an inverse Fourier transformation of the partial RSF over a $R + \Delta R$ range of [0–5.4 Å] by excluding peak F. Figure 14a shows that exclusion of the Fe-Fe3 contribution substantially modifies the spectral shape. This modification is statistically significant because the R_p value between the two spectra is equal to 1.36×10^{-4}, which is approximately an order of magnitude greater than the estimated precision for the spectral measurement ($R_p = 11 \times 10^{-4}$, Table 1). The most spectacular modification is observed at k = 7.9 Å^{-1}, where the appearance of Fe-Fe3 pairs at R ~6.2 Å yields a marked node pattern that reduces the amplitude of the wave oscillation. Given the high quality of EXAFS spectra, this spectral feature has undoubtedly a structural origin. A similar analysis was conducted for the perpendicular orientation. This treatment revealed that the Fe-O3 contribution is responsible for the shoulder at k = 3.4 Å^{-1} observed in Figure 7d. The location of the spectral signature for the O3 shell at lower k (3.4 Å^{-1}) than the Fe3 contribution (7.9 Å^{-1}) results from the difference in shape of $A_O(k)$ and $A_{Fe}(k)$ functions as shown in Figure 2 of Manceau et al. (2000).

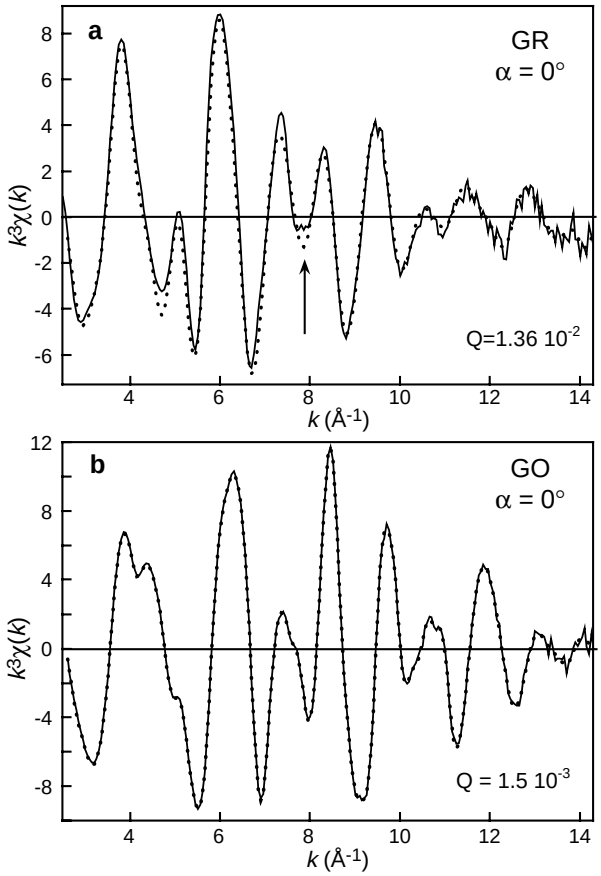

FIGURE 14. (**a**) Experimental k^3-weighted EXAFS spectrum for GR at α = 0° (solid line), and Fourier filtered $k^3\chi(\alpha = 0°)$ function for GR in the [0, 5.4 Å] $R + \Delta R$ interval (dotted line). (**b**) Experimental k^3-weighted EXAFS spectrum for GO at α = 0° (solid line), and Fourier filtered $k^3\chi(\alpha = 0°)$ function for GO in the [0–10 Å] $R + \Delta R$ interval (dotted line).

Another important difference in the in-plane FT[$k^n\chi(\alpha = 0°$] functions for GR and GO was identified above 6 Å. Within this more distant range (Fig. 15a) a peak at $R + \Delta R$ = 8.6 Å (G) is observed for GO, which is approximately twice as intense as the surrounding background signal. Note that this peak is absent in GR. The structural reality of this peak was further assessed by comparing the full experimental $k^3\chi(\alpha = 0°)$ function with that recalculated from the RSF by back-transforming the [0–8.3 Å] range. The two EXAFS spectra differ only by the intensity of several oscillations (data not shown). The lack of a distinct spectral feature in k space attributed to peak G, in contrast to that observed previously for peak F (Fig. 14a), may be explained by the overall low contribution that this atomic shell makes to the whole EXAFS spectrum. Experimental and recalculated spectra differed, however, by $R_p = 22 \times 10^{-4}$, which is 2.5 times higher than the estimated experimental precision (8×10^{-4}, Table 1). This difference is due to RSFs peaks, which were not included in the back FT window, and that are located in the [8.3–∑ Å] range. In this domain, RSFs peaks arise from the Fourier transformation of the medium to high frequency signal in the EXAFS spectrum. This signal originates partly from the statistical high frequency counting noise of the measurement, but still includes some structural contributions from distant Fe shells. Thus, for the sake of completeness in our assessment of the structural origin of peak G, the entire EXAFS spectrum of GO was recalculated over the whole [0–10 Å] $R + \Delta R$ window, and compared to the experimental spectrum (Fig. 14b). The amplitudes of oscillations are similar, the only difference being that the recalculated spectrum has no high frequency noise. The two spectra in Figure 14b differ by $R_p = 15 \times 10^{-4}$, which should be *a priori* identical to that determined from the linearization procedure (8×10^{-4}, Table 1). One reason for the difference observed is that the [10, ∞ Å] range contains minor Fe-Fe contributions that are progressively lost in background noise, and which are not taken into account when the Fourier transform is performed in the [0–10 Å] range. From these considerations, peak G is likely structural and can be attributed to the Fe5 shell at $R = b$ = 9.15 Å (Fig. 13). The presence of this peak in the oxidized nontronite, despite the long distance, is explained by the existence of high order MS paths along the Fe-Fe1-Fe5, and Fe-Fe3-Fe5 chains. Consequently, the disappearance of peak G in GR indicates that the reduced sample has no, or very few, Fe atoms in the 5th Fe shell. Thus, that the formation of trioctahedral Fe^{2+} clusters is globally realized by occupancy of formerly vacant octahedra in the Fe1 shell, and by a concomitant departure of Fe atoms from the Fe5 shell. The Fe^{2+} domains therefore have a limited lateral extension, and the migration of Fe^{2+} atoms should be restricted to short distance, for instance from cis-occupied to adjacent trans-vacant sites.

Structural parameters of reduced nontronite. Three Fe shells were identified in the RSF of reduced nontronite at α = 0°: Fe1 (B), Fe2 (E), and Fe3 (F) (Fig. 12). Equation 9 in Manceau

et al. (2000) shows that for a given atomic pair *ij* (i.e., given ϕ_{ij} function), the wave frequency of χ_{ij} is determined by the distance (*R*) separating atoms *i* and *j*. Thus, the comparison of wave frequencies for Fe-Fe1 and Fe-Fe2 pairs in oxidized and reduced samples provides insight on the modification of distances to different Fe shells during the redox reaction. This analysis is generally achieved by superimposing patrial EXAFS spectra obtained by Fourier back-trasnsforming specific RSF peaks. Alternatively, comparison of the imaginary parts of the forward ($k \rightarrow R$) Fourier transform may be used (Teo 1986). The imaginary parts for GO and GR closely overlap at $R + \Delta R = 2.7$ Å (arrow 1 in Figs. 15b and 15c) and 4.7 Å (arrow 3), but the phase of GR progressively shifts to the right when *R* increases (arrows 2 and 4). In oxidized Garfield, Fe atoms in the Fe1 and Fe2 shells are located at the coherent distances of 3.05 Å (*b*/3) and 5.28 Å (*a*), respectively, from the central Fe. Consequently, the imaginary part below peaks B and E in GO possess a *unique* frequency. Thus, the progressive shift in phase observed in GR indicates that Fe-Fe distances are incoherent within the Fe1 and Fe2 shells. Peak E in GR is a doublet (Fig. 15a), which suggests a bimodal distribution of the Fe-Fe2 distances. The incoherence of the Fe-Fe1,2 distances is a source of structural disorder, and explains the weakening of peaks B and E (Fig. 15b) in the reduced state relative to the oxidized state. However, the amplitude loss is more pronounced on FT[$k^3\chi(\alpha = 0°]$ than on FT[$k\chi$ ($\alpha = 0°$] functions (Figs. 15b and 15c). To understand this difference, we compare $k^3\chi_{Fe1}$ and $k^3\chi_{Fe2}$ functions in the two redox states (Figs. 16a and 17a).

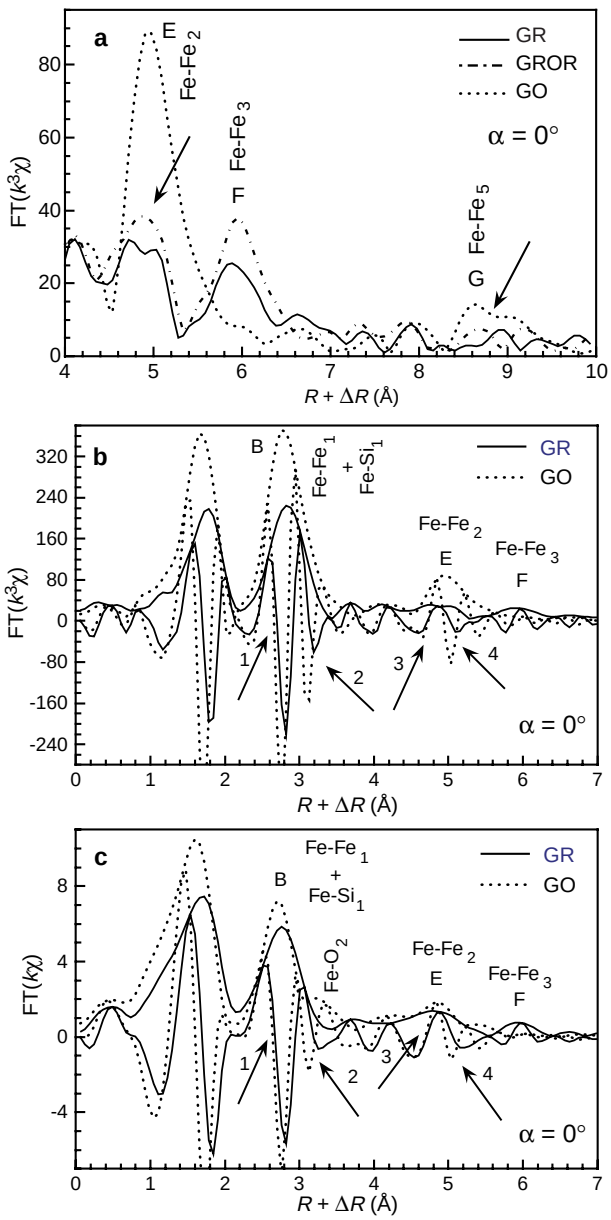

FIGURE 15. (**a**) Expanded view of the 4–10 Å interval of k^3-weighted RSFs functions in the parallel orientation for GO, GR and GROR. (**b**, **c**) Modulus and imaginary part of Fourier transforms for GR and GO at $\alpha = 0°$. (**b**) k^3-weighting. (**c**) *k*-weighting.

The wave envelopes of these two functions differ substantially. For GO, the $k^3\chi_{Fe1}$ and $k^3\chi_{Fe2}$ spectra have the characteristics of a single Fe shell contribution with an amplitude maximum at 8 $Å^{-1}$ as predicted from theory (see Fig. 1 in Manceau et al. 2000). The assumption of unique structural distances of 3.05 Å (*b*/3) and 5.28 Å (*a*) in Fe1 and Fe2 shells yielded good fits to these spectra with R_p values of 0.021 (Manceau et al. 2000) and 0.022 (Fig. 16b). However, the two $k^3\chi_{Fe}$ contributions of GR exhibit a different spectral shape with a maximum at low *k* (4–6 $Å^{-1}$) followed by a rapid damping of the amplitude at increasing *k* (Figs. 16a and17a). A similar observation was made for $k^3\chi_{Tet1}$ in GR (Fig. 11a) as a result of the incoherence of the Fe-(Si,Al)1 distances. Thus, the dispersion of interatomic distances observed at $\alpha = 90°$ clearly is not limited to the Tet1 shell, but extends also to the Fe1 and Fe2 shells. This in-plane and out-of-plane structural disorder detected on $k^3\chi_{Tet1}$ and $k^3\chi_{Fe1,2}$ functions accounts for the severe damping in amplitude of the whole EXAFS spectra (Figs. 7c and 7d) for reduced samples relative to GO. For instance, the amplitude of $k^3\chi_{Fe1}$ for GO equals 2.8 (arbitrary unit) at 11.8 $Å^{-1}$ (arrow in Fig. 16a), and the amplitude of the whole EXAFS spectrum at the same *k* value is 4.8 (Fig. 7c). This comparison indicates that the Fe1 shell alone contributes as much as 56% of the entire EXAFS signal in the high *k* region at $\alpha = 0°$. Therefore, the high wave-vector range of the raw EXAFS spectra must be dominated by Fe-Fe interactions at $\alpha = 0°$ (i.e., in-plane), and by the Fe-Tet1 at $\alpha = 90°$ (i.e., out-of-plane). This analysis indicates, therefore, that the large damping of the EXAFS signal in the reduced state results from the variation of interatomic Fe-Tet and Fe-Fe distances in GR.

The damping of the Fe-Fe signal is more apparent on k^3-weighted than *k*-weighted Fourier transforms (Fig. 15). The reason for this behavior is now evident when we compare $k^3\chi_{Fe1,2}$ spectra for GO and GR (Figs. 16a and 17a). FT[$k^n\chi$] functions are obtained by integrating $k^n\chi$ spectra over *k* (Eq. 10 in Manceau et al. 2000) and, consequently, the structural Fe-Fe disorder, apparent at $k > \sim 6$ $Å^{-1}$, is emphasized when FTs are performed on $k^3\chi$. In contrast, multiplication of χ by *k* decreases the weight of the high *k* region relative to the low *k* region. In this case, GR has a slightly higher $\chi_{Fe1,2}$ amplitude than GO. Thus, less emphasis is given to in-plane structural disorder in the *k*-weighting.

Obviously, the Fe1 and Fe2 shells in GR include several Fe-Fe distances. The assumption of a single Fe1 shell of 4.9 Fe at $<R>$ = 3.12 Å ($\Delta\sigma$ = 0.03 Å) provided a reasonable fit to χ_{Fe1} (R_p = 0.004, Fig. 16c). In this simulation, the distribution of distance was modelled by assuming a Gaussian distribution of distances ($\Delta\sigma$), and the Fe1 shell was fitted by 4.9 Fe located at an average distance of 3.12 Å with a continuous distribution of 0.03 Å half-width. The distribution of the Fe-Fe1 distances is too small to be resolved, and the fit would be insignificantly improved by assuming two discrete Fe-Fe distances. The precision of N_{Fe1} was estimated by varying σ:$\Delta\sigma$ = 0.02 Å yielded N_{Fe1} = 3.9 and R_p = 0.012, and $\Delta\sigma$ = 0.04 Å yielded N_{Fe1} = 6.0 and R_p = 0.010. When R_p was 2.5 to 3.0 times greater than its optimal value, the spectral fit was visually degraded, leading to the conclusion that the 3.9–6.0 interval represents the maximum range for the variation of N_{Fe1} (±20%), N_{Fe1} likely being between 4.5 and 5.4 (±10%). Individual Fe-Fe distances are less overlapping in the Fe2 than in the Fe1 shell, as attested by the splitting of peak E (Fig. 15a), and the node pattern at ~9 Å^{-1} (Fig. 17a). This wave node was satisfactorily reproduced by assuming two discrete sub-shells composed of ~1.7 Fe at 4.86 Å ($\Delta\sigma$ = 0.03 Å) and ~3.4 Fe at 5.38 Å ($\Delta\sigma$ = 0.03 Å) (Fig. 17b). In general, the precision of N decreases with distance from the central atom, and in the present case has been estimated to be ±1 Fe. The relative precision is better, and we may estimate that the long distance sub-shell at 5.38 Å contains 2 to 3 times more Fe than the closer shell at 4.86 Å.

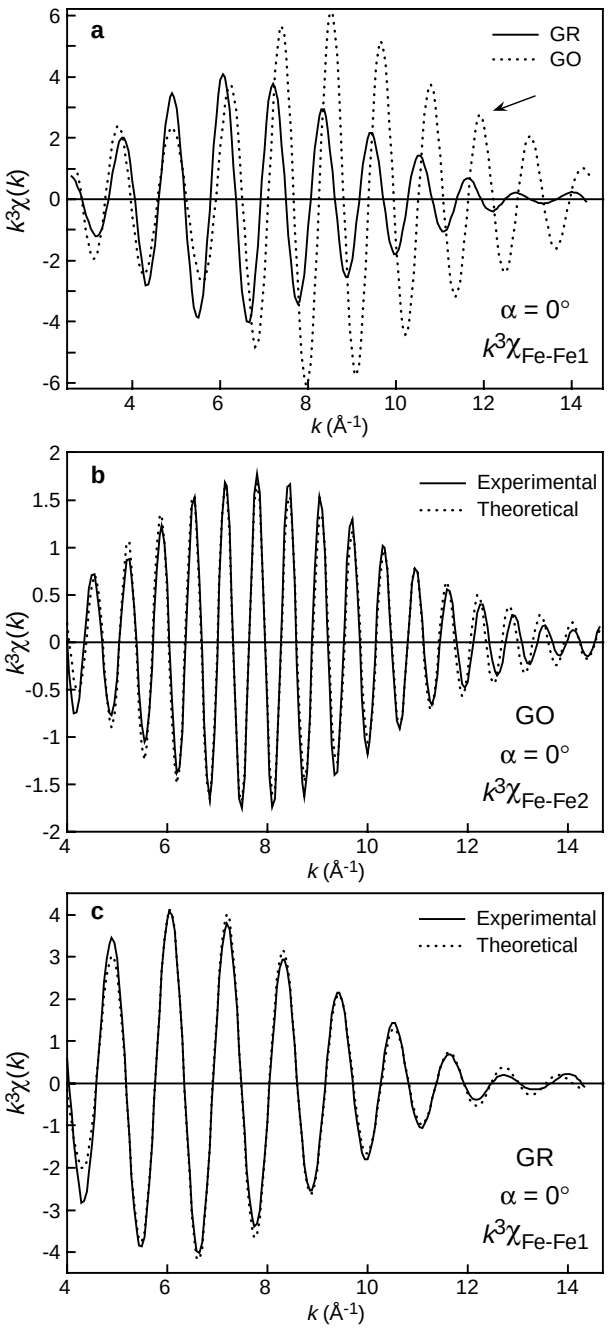

FIGURE 16. (**a**) Comparison of Fourier filtered $\chi_{Fe\text{-}Fe1}(\alpha = 0°)$ functions for GR and GO. (**b**) Best one shell spectral fit of $\chi_{Fe\text{-}Fe2}(\alpha = 0°)$ for GO. (**c**) Best one-shell spectral fit of filtered $\chi_{Fe\text{-}Fe1}(\alpha = 0°)$ for GR.

The wave envelope of the third Fe shell ($k^3\chi_{Fe3}$) for GR (corresponding to peak F in Fig. 15a) shown in Figure 17c differs unexpectedly from GR $k^3\chi_{Fe2}$, but resembles GO $k^3\chi_{Fe2}$ (Fig. 17a), indicating that the Fe-Fe3 distances are coherent. This finding was confirmed by overlaying GO $k^3\chi_{Fe2}$ and GR $k^3\chi_{Fe3}$ (Fig. 17d), and by calculating the theoretical amplitude function $k^3A_{Fe2}(k) = k^3F_{Fe}(k) \exp(-2\sigma^2k^2) \exp[-2R/\lambda(k)]$ for a single Fe shell contribution with the FEFF 7.02 code (details are in Manceau et al. 2000). The experimental $k^3\chi_{Fe2,3}$ curve envelopes and $k^3A_{Fe2}(k)$ have the same line shape (Fig. 17d), which proves that the Fe3 shell in sample GR cannot be split into two sub-shells, as was the case for the Fe2 shell. Therefore, the structural disorder observed in the Fe1 shell, and predominantly in the Fe2 shell of GR, is less important in the Fe3 shell. Because the Fe1 and Fe3 shells are aligned along the [010], [310], [$\bar{3}$10] directions, whereas the Fe2 shell is oriented along the [100], [110], [1$\bar{1}$0] directions, the disorder induced by reduction of structural Fe is anisotropic and is more pronounced in directions of the Fe2 shell (Fig. 13a).

Structural differences between GR and GROR samples

GR and GROR have similar in-plane and out-of-plane EXAFS spectra (Figs. 7c and 7d), differing only by a slight increase in amplitude of the twice reduced sample. To interpret these spectral differences we compare (Fig. 18) the two RSF functions at α = 0° and 90°. The two RSFs have, for each orientation, the same peaks at the same distances, which means that the two reduced samples have the same overall structure. But, as was predicted from amplitude differences of $k^3\chi$ (Fig. 7), GROR has generally more intense RSF peaks, and thus a higher short- to mid-range structural order than GR. The fact that peaks A and B are more intense in GROR than in GR both at α = 0° and 90° implies that this must be also the case at α = 35° and, consequently, that these RSFs differences have a structural rather than textural, origin. The increase in peak amplitude does not uniformly affect the various atomic pair contributions and is predominantly observed for the O1, Fe1, Fe2, Fe3, and to some extent the Si1, shells, which suggests that Fe atoms are partitioned differently in the two samples. Proper structural inter-

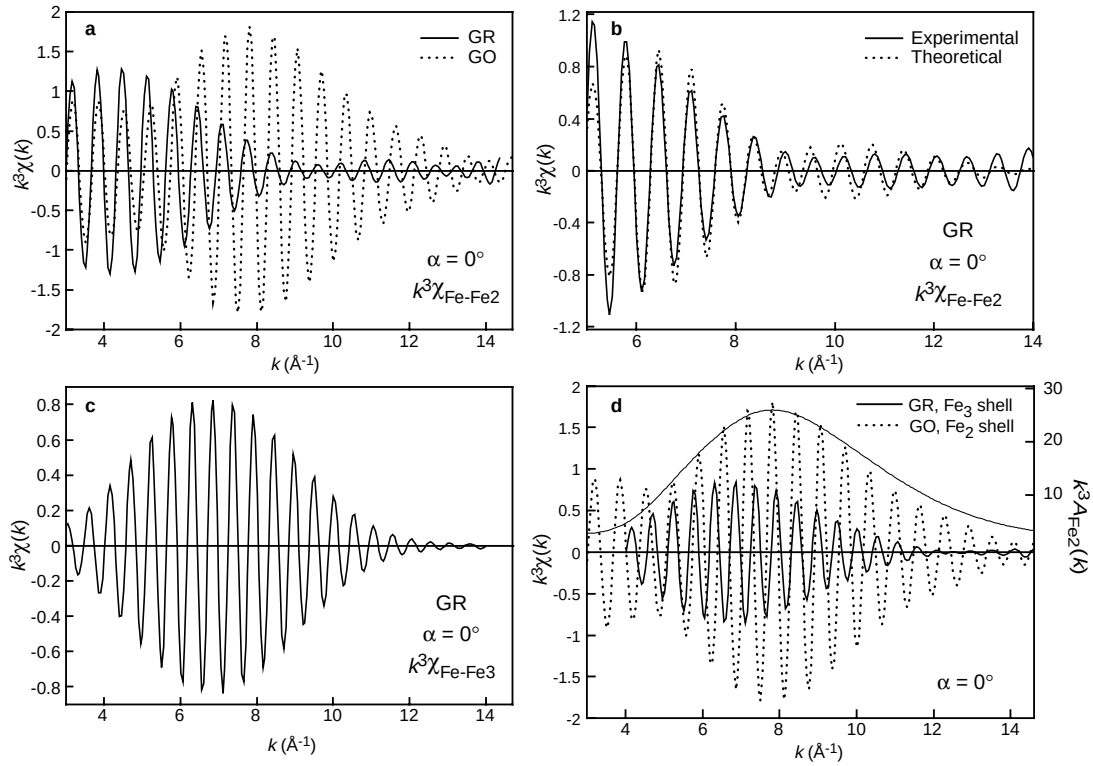

FIGURE 17. (**a**) Fourier-filtered $k^3\chi_{Fe\text{-}Fe2}$ ($\alpha = 0°$) contributions to EXAFS for GR and GO. (**b**) Best two-shell fit of $k^3\chi_{Fe\text{-}Fe2}$ ($\alpha = 0°$) for GR. (**c**) Fourier-filtered $k^3\chi_{Fe\text{-}Fe3}$ ($\alpha = 0°$) function for GR. (**d**) $k^3\chi_{Fe\text{-}Fe2}$ ($\alpha = 0°$) function for GO, $k^3\chi_{Fe\text{-}Fe3}$ ($\alpha = 0°$) function for GR, and $k^3A_{Fe2}(k) = k^3F_{Fe}(k) \exp(-2\sigma^2k^2) \exp[-2R/\lambda(k)]$ function calculated with FEFF 7.02 (Rehr et al. 1991). $\sigma = 0.11$ Å

pretation of the spectra requires us to know whether the increased amplitude results from a reduction of the incoherency of interatomic distances, or from an increase in the number of nearest atomic neighbors in the successive atomic shells. In the former case, the Fe^{2+} domains would have the same size but a greater structural order, whereas in the latter they would be larger. Evidence is given below that GROR has, in all likelihood, larger and more highly ordered trioctahedral Fe^{2+} clusters than GR.

Higher order for Fe^{2+} domains is deduced from considering the O1 and Fe2 shells. Because Fe^{2+} is sixfold coordinated in the reduced samples, the enhancement of first RSF peaks in GROR at $\alpha = 0°$ and 90° attests that the distribution of bond lengths of the coordination polyhedra of Fe^{2+} become more symmetrical after two reductions. Also, peak E is no longer split after the second reduction (Fig. 15a). The best fit to this contribution yielded ~1.7 Fe at 4.86 Å ($\Delta\sigma = 0.03$ Å) and ~4.5 Fe at 5.38 Å ($\Delta\sigma = 0.03$ Å) as compared to ~1.7 Fe at 4.86 Å ($\Delta\sigma = 0.03$ Å) and ~3.4 Fe at 5.38 Å ($\Delta\sigma = 0.03$ Å) for GR (Fig. 17b). Thus, GROR contains more Fe atoms in its second shell than GR and a lower proportion of short distance Fe-Fe2 pairs.

Arguments in favor of a larger size of Fe^{2+} clusters in GROR are based on the analysis of peaks F (Fe3) and G (Fe5). The Fe3 shell was shown above to be more coherent than the Fe2, consequently the greater amplitude observed for peak F (Figs. 15a and 18a) is almost certainly due to an increase in N_{Fe3} and, accordingly, in the size of trioctahedral clusters. The RSF for GROR (Fig. 15a) contains a weak bump where peak G is expected, which may be interpreted as pertaining to Fe5 in-plane shell. The low intensity of this feature, however, weakens this argument.

Indirect considerations support the presence of Fe atoms in the 5th in-plane shell. The structural disorder recurrently observed during the spectral analysis of sample GR most likely originates from a limited size of Fe^{2+} clusters, which implies that a large number of Fe atoms occur at the border of the trioctahedral domains. As shown below, these surface Fe atoms have different coordination and local structure compared to the inner Fe atoms. Consequently, the general enhancement of the O1, Fe1, Fe2, and Si1 shell signals observed after the second reduction (Fig. 18) very likely results from an increase in the size of the Fe^{2+} clusters. Under these conditions, the Fe5 in-plane shell should necessarily contain a minimum number of Fe atoms.

DISCUSSION

Structural model for reduced nontronite

Three results are crucial to understanding structural changes which occur during the reduction of Fe^{3+} to Fe^{2+} in nontronites. (1) Fe^{3+} cations preserve their sixfold coordination. Earlier works suggested that structural Fe^{3+} undergoes a sixfold to fivefold transformation (Roth and Tullock 1973; Stucki and roth

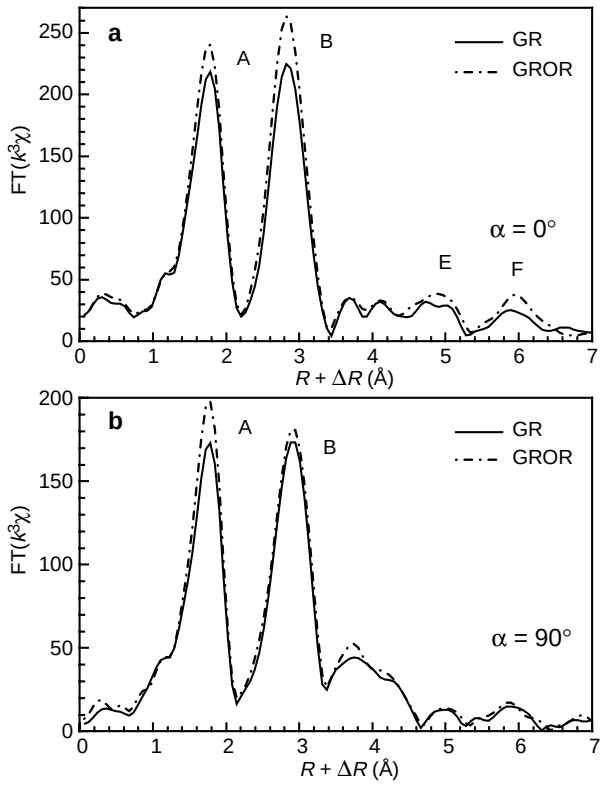

FIGURE 18. k^3-weighted RSFs functions for GR and GROR. (**a**) parallel orientation. (**b**) normal orientation.

1976, 1977). (2) In the reduced state, Garfield nontronite contains at least three adjacent edge-sharing Fe octahedra along the [010], [310], and [$\bar{3}$10] directions, whereas the original oxidized sample contained only two. This result provides evidence that some Fe atoms migrated from cis- to trans-sites to form the short—Fe-Fe-Fe—chains typical of trioctahedral clay structures. The structural modification of the octahedral sheet due to reduction suppresses the corrugation of basal oxygen planes, typical of dioctahedral smectites, resulting in a flat basal surface, as in trioctahedral layer silicates (Lee and Guggenheim 1981). The migration of Fe during the reduction process is supported by P-EXAFS, infrared spectroscopy, and by X-ray diffraction as the simulation of the XRD pattern for GR showed that 28% ± 5% of Fe^{2+} cations are in trans sites, whereas in oxidized nontronite trans sites are entirely vacant (Manceau et al. 2000). (3) The incoherency of the Fe-Fe1 and Fe-Fe2 distances is greater in the reduced nontronite than in trioctahedral structures. These structural modifications are accompanied by a loss of structural OH groups (Lear and Stucki 1985; Rozenson and Heller-Kallai 1978; Stucki 1988).

We now construct a structural model, which is compatible with all available structural data. The lattice fragment shown in Figure 19a corresponds to a tv octahedral sheet in which a pair of Fe^{3+} cations in adjacent cis octahedra is reduced, and the pair of OH groups coordinated to the reduced Fe atoms is protonated by solution H^+ according to $2(OH)^-_{layer} + 2H^+_{sol} \rightarrow 2H_2O$. Because Fe atoms remain sixfold coordinated, the reduction of Fe^{3+} and protonation of OH groups should be accompanied by the following two phenomena: (1) a migration of reduced Fe^{2+} from its original cis site to the nearest vacant trans site along [010], and (2) a dehydroxylation of the initial octahedral sheet due to the protonation of OH groups. This structural transformation results in the formation of a hole consisting of four empty "octahedra" (Figs. 19b and 19c) and cation migration resulting in the nucleation of trioctahedral clusters. One of the most important consequence of this cation migration is the formation around the hole of octahedral edge-sharing Fe chains aligned along the [010], [310], and [$\bar{3}$10] directions.

Iron octahedra nearest to the hole should be deformed because the local charge balance is disturbed by the new distribution of Fe atoms. The intensity of this perturbation can be estimated by using Pauling's (1929) rule that the sum of bond valences received by an ion from its coordinating atoms should be nearly equal to its formal charge. The bond strength in valence unit (v.u.) between an ion and its ligands is obtained by dividing the formal valence by the coordination number. If the number of coordinating ions decreases, the increase in partial charge must be compensated by a shortening of bond lengths because the strength of a bond increases exponentially when the bond distance diminishes. This change of the cation-anion distance is actually achieved by a displacement of atoms from their ideal crystallographic position (Brown 1981; Brown and Shannon 1973).

Consider now the distribution of bond valences received by bridging surface O atoms (O_{ext}) located at the interface between Fe^{2+} clusters and holes (Fig. 19c). Among the 14 border anions of a given hole, four of them, labelled 3, 6, 10, and 13, are coordinated to one octahedral (Fe) and one tetrahedral (Si,Al) cation. The sum of bond strengths received by each of them, assuming non-distorted polyhedra, varies from 1.33 v.u. (1.00 + 0.33) to 1.08 v.u. (0.75 + 0.33), depending on the nature (Si vs. Al) of the tetrahedral cation. Another group of border anions, labelled 2, 4, 5, 7, 9, 11, 12, and 14, is coordinated to two Fe^{2+} edge-sharing octahedra and one tetrahedra. Their bond strength lies between 1.66 and 1.41 v.u. The third group of anions corresponds to O atoms bonded to two Fe^{2+} and one proton (O_{ext}), labelled 1 and 8, and are located at the termination of holes. Their bond strength varies between 1.66 v.u. (0.66 + 1.00) and 1.46 v.u. (0.66 + 0.80), depending on the strength of the O-H bond (Brown 1976). All these surface O atoms are undersaturated to variable degrees with respect to fully satisified oxygen (2.0 v.u.). The charge compensation of O_{ext} is probably realized by the sorption of protons from solution and by a shortening of the Fe-O_{ext} distances. The directions of displacement of Fe atoms towards the undersaturated surface O atoms are indicated in Figure 19c by arrows. These displacements lower the coherency of the Fe-Fe distances; specifically Fe-Fe2 pairs oriented along the *a* axis are shortened in comparison to the non relaxed bulk structure.

This mechanism of charge compensation accounts for the short Fe-Fe2 distance of 4.86 Å determined by EXAFS in GR and GROR. However, the maximum gain in charge expected from the displacement of border Fe atoms is of a few tenths of

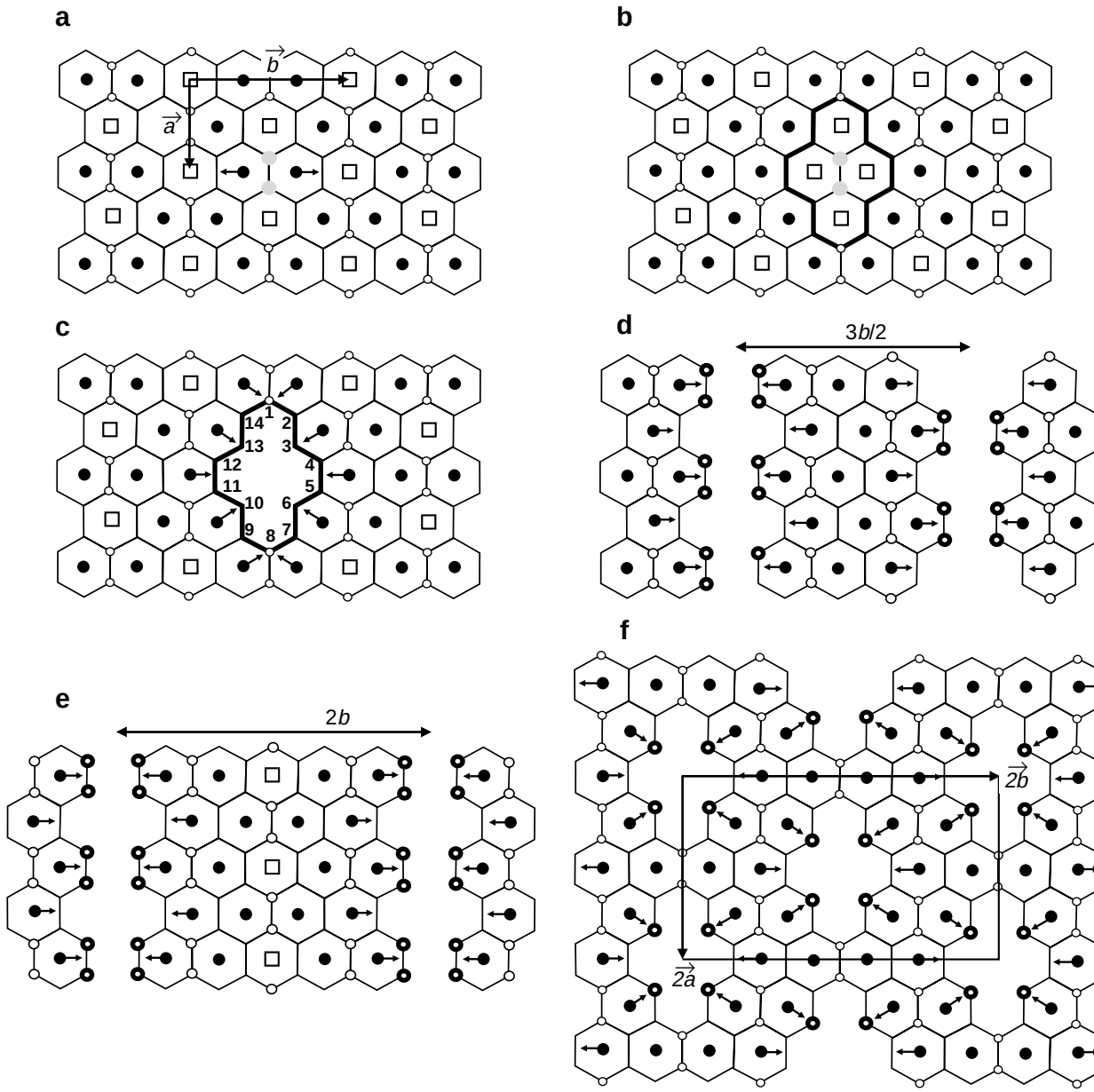

FIGURE 19. Various structural models for the distribution of Fe^{2+} in the octahedral sheet of reduced nontronite. OH, Fe, and vacant sites are represented by open circles, filled circles, and squares, respectively. In **a** and **b**, H_2O molecules are in gray.

v.u. (Manceau and Gates 1997), which is insufficient to fully balance the charge deficit residing at the first group of greatly undersaturated (0.67–0.92 v.u.) O atoms (3, 6, 10, 13). The bond valence sum of these O atoms might be increased through by the incorporation of H^+ from solution, because the O-H bond strength varies between 0.7 and 1.0 v.u. depending on the presence and strength of H bonds (Brown 1976). The proposed model for the migration of Fe^{2+} from cis to trans sites during the reduction reaction appears to account for three important experimental findings: (1) the formation of trioctahedral clusters, (2) the high structural disorder of the octahedral sheet created by the incoherency of the Fe-Fe distances, and (3) the protonation of the structure following the initial dehydroxylation (Lear and Stucki 1995).

We examine now how the local structural transformation develops at a medium scale. Imagine that the sequence of reactions described in Figure 19a to 19c is replicated along [010] to form empty channels delimiting trioctahedral Fe^{2+} ribbons (Fig. 19d). Of course, the size and composition of Fe^{2+} clusters depend on the mutual arrangement and length of empty holes. Possible structural models are comprised between two extreme cases. In the first case, holes are elongated along *a* and form

infinite channels (Fig. 19d), whereas in the second case, holes have a four-octahedra size and are based-centered with maximum density (Fig. 19f). Intermediate models may be constructed by varying the spacing between channels or the length of holes along [100]. Figures 19d and 19e represent two models of infinite channels separated by $L = 3b/2$ and $2b$. In the former, one third of Fe^{2+} octahedra are located in the middle of clusters, and share 6 edges with nearest octahedra; the other two thirds are on the border and share 3 or 5 edges. For this distribution pattern $<N_{Fe1}> = 4.7$, which agrees well with the EXAFS value of 4.9 for GR. When $L > 3b/2$, Fe^{2+} clusters contain tv octahedra, and $<N_{Fe1}>$ is always lower than 4.7. For instance, the pattern of Figure 19e has $<N_{Fe1}> = 4.25$. Variations with larger L and lower $<N_{Fe1}>$ can exist, until $L = \infty$, then $<N_{Fe1}> = 3$ as in a dioctahedral layer like GO (Fig. 19a). Thus, if infinite channels exist, they should be separated by $3b/2$, so that Fe^{2+} clusters contain no tv positions.

Despite the agreement between calculated N_{Fe1} in the $3b/2$ model (4.7) and experimental data (4.9), this solution must be rejected because it fails to explain the structural disorder observed in the Fe2 shell. The direction of arrows in Figure 19d indicates that the average Fe-Fe2 distances must be equal to at least a = 5.32 Å, which is inconsistent with the bimodal distribution of EXAFS values: d(Fe-Fe2) = 4.86 Å and 5.38 Å. A significant portion of shorter Fe-Fe2 distances in GR is indicated by the splitting of peak E in Figure 15a, which exhibits one maximum at a shorter $R + \Delta R$ value than GO. This implies that a proportion of Fe atoms has moved in convergent directions (see Fig. 19c and compare with Fig. 19d where all displacements are parallel). The only way to satisfy the constrains of experimental data is to reduce the length of channels. If the size of empty channels is limited to four-octahedra holes, as in Figure 19f, and if these holes are distributed according to a based-centered superstructure with $\boldsymbol{A} = 2\boldsymbol{a}$ and $\boldsymbol{B} = 2\boldsymbol{b}$, then 40% of the Fe-Fe2 distances in reduced structural fragments are shorter than $a = 5.32$ Å, in agreement with the relative number of Fe2 atoms within each sub-shell (1.7 vs. 3.4, Fig. 17b). In this model, however, the Fe1 shell contains 4.25 Fe-Fe1 pairs instead of 4.9 observed in GR.

The various possible models, based on the existence of infinite channels as well as of four-octahedra holes, showed that N_{Fe1} is maximized with infinite channels separated by $L = 3b/2$, whereas the octahedral sheet distortion is optimal with four-octahedra holes distributed according to a based-centered superstructure. Consequently, a compromise structure between these two extremes should be made. Figures 20a and 20b represent two such structures, one of which contains holes of seven vacant octahedra of $11a/4$ length, and the other holes of ten vacant octahedra with length = $15a/4$. The holes were distributed with the superstructure $\boldsymbol{A} = (3\boldsymbol{a}+\boldsymbol{b})/2$ and $\boldsymbol{B} = (\boldsymbol{a}+3\boldsymbol{b})/2$ in the former model, and $\boldsymbol{A} = (7\boldsymbol{a}+\boldsymbol{b})/2$ and $\boldsymbol{B} = (\boldsymbol{a}+3\boldsymbol{b})/2$ in the latter, to avoid the occurrence of isolated vacant octahedra. The Fe1 shells contain 4.4 and 4.5 Fe-Fe1 pairs, respectively, both of which are within the 10% precision of the EXAFS value of 4.9. These new models also contain average Fe-Fe2 distances shorter than $a = 5.32$ Å, but their proportions are now 30% (Fig. 20a) and 15% (Fig. 20b) as compared to 40% in the previous model (Fig. 19f). The first proportion is compatible with the relative amount of Fe atoms within each Fe2 sub-shell determined by EXAFS for GR [(1.7/(1.7 + 3.4) = 33%)] and GROR [(1.7/(1.7 + 4.5) = 27%)]. The occupancy of the M1 site is 25% in the model represented in Figure 19f, 28% in the model in Figure 20a, and 30% in the model in Figure 20b. In pure trioctahedral octahedral sheets the M1 occupancy is 1/3 because the unit cell contains two M2 sites and one M1 site. Thus, the larger the size of the Fe^{2+} domains, the closer Fe^{2+} cations will be partitioned as in a pure trioctahedral framework.

In comparison to GR, the re-reduced sample, GROR, has larger and less disordered Fe^{2+} clusters. Figure 20a shows that nearest holes are separated by only one or two octahedra. Thus, for energetics reasons (i.e., decrease of the layer distortion), holes conceivably will tend to coalesce during the cyclic GR $\rightarrow$ GRO $\rightarrow$ GROR transformation, while Fe^{2+} octahedra of the hole walls will contribute Fe^{2+} clusters which will progressively increase in size along with the number of reduction-oxidation cycles. Finally, our models depicted in Figures 19f and 20 show that in average Fe-Fe distances are longer in the b than in the a direction due to the displacement of Fe atoms towards empty slits. This anisotropic distortion accounts for the departure from the hexagonal to orthogonal symmetry of the octahedral sheet as determined by XRD because $b/a > \sqrt{3}$.

Structural formula for reduced nontronite

Despite the fact that the complete chemical composition of reduced Garfield nontronite is lacking, a tentative structural formula, based on the model presented in Figure 20a, can be determined using the layer charge considerations and the known Na content. As a consequence of reducing Fe^{3+} to Fe^{2+}, the layers accumulate negative charge, which is compensated by the sorption of Na^+ and H^+ ions from solution. Na^+ occupies interlayer sites, whereas H^+ lowers the negative layer charge by transforming structural OH^- into water molecules. This reaction accompanies the migration of Fe^{2+} ions, and results in the formation of holes. But even this reaction is insufficient to attain full electroneutrality of the layer, and an excess of negative charge remains in an amount that depends on the size and distribution of empty holes or channels. To illustrate this point, let us compare the anionic composition of the framework for the various strutural models represented in Figure 19 and 20. It is equal to $O_{20}(OH)_{3.0}$ per unit cell in Figure 19f; $O_{20}(OH)_{2.86}$ in Figure 20a; $O_{20}(OH)_{2.80}$ in Figure 20b; and $O_{20}(OH)_{2.70}$ in Figure 19d, as compared to $O_{20}(OH)_4$ in oxidized nontronite. Thus, after dehydroxylation the 2:1 layers have a total negative charge of 43 v.u., 42.86 v.u., 42.80 v.u., and 42.70 v.u. per unit cell, respectively. All structural models have instead the same cation composition $Na_{1.30}[Si_{7.22}Al_{0.78}]\ [Fe^{2+}_{3.65}Al_{0.32}Mg_{0.04}]$, and hence the same total positive charge of 40.86 v.u.. Therefore, to achieve full compensation of the negative layer charge, 1.84 to 2.14 H^+ should be incorporated from solution depending on the model used, in addition to the initial protons needed for the dehydroxylation. Thus, if this mechanism of charge compensation is valid, then the structural formulae for the idealized structural models of Figure 19f and 20a can be written respectively:

$$H_{2.14}Na_{1.30}[Si_{7.22}Al_{0.78}][Fe^{2+}_{3.65}Al_{0.32}Mg_{0.04}]O_{20}(OH)_{3.0}$$

$$H_{2.0}Na_{1.30}[Si_{7.22}Al_{0.78}][Fe^{2+}_{3.65}Al_{0.32}Mg_{0.04}]O_{20}(OH)_{2.86}$$

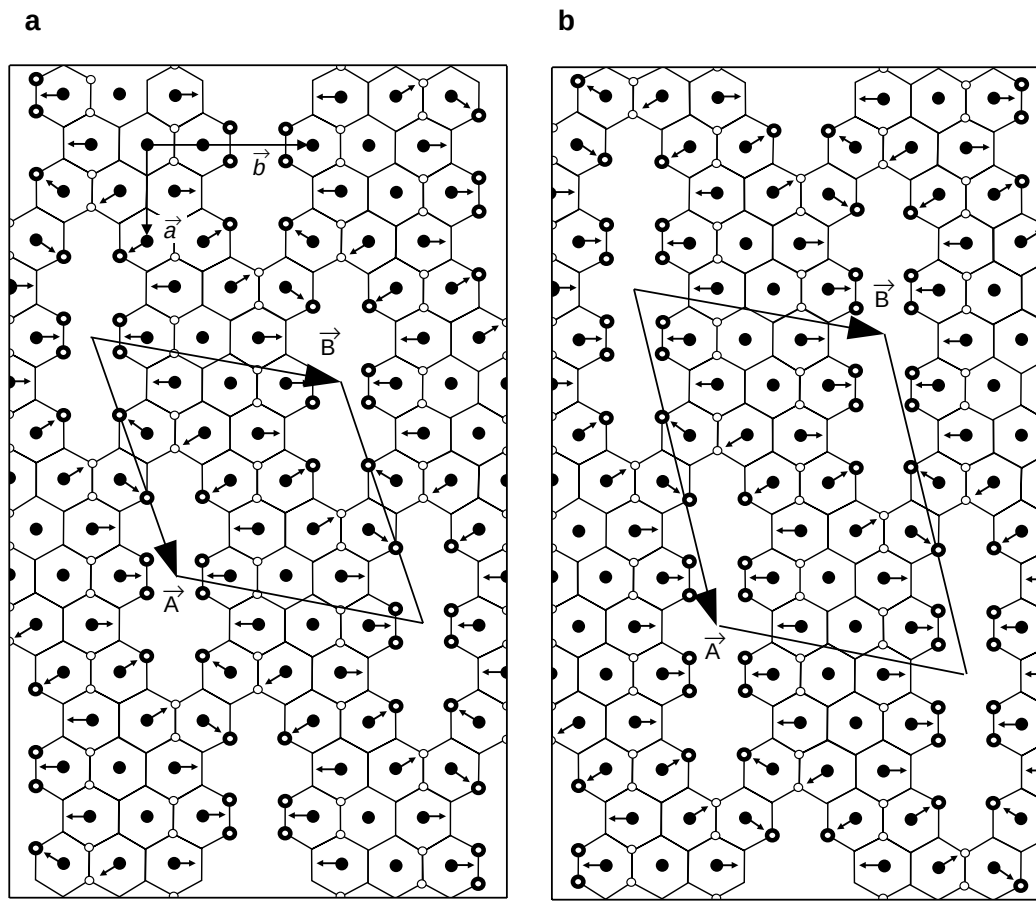

FIGURE 20. Two possibilities for the structure of the octahedral sheet of reduced Garfield nontronite.

Obviously an important question to consider is how, and where, are these excess protons incorporated in the structure. As discussed previously, they are likely located within the layer holes where they compensate the excess of negative charge borne by bordering O atoms (O_{ext}). If each of the most undersaturated O_{ext} groups take up one proton, then 8 H^+ will be present in each supercell in Figures 19f and 20a, which corresponds to 2.0 and 2.3 H^+ per unit cell, respectively. To achieve the desired amount of 2.14 and 2.0 H^+ per unit cell, to agree with structural formulae, every supercell should contain 8.56 H^+ in the four-octahedra hole model and 7 H^+ in the seven-octahedra hole model. Thus, in the first model (Fig. 19f) the amount of H^+ predicted by the structural formula is higher than the expected amount, whereas the reverse is true for the second model. The actual structure of GR is likely more complex than that idealized in these two models, and it can be conceptually described by the co-existence of four- and seven-octahedra holes. As an example, nontronite layer containing an equal proportion of each structural unit would have the following structural formula:

$$H_{2.07}Na_{1.30}[Si_{7.22}Al_{0.78}][Fe^{2+}_{3.65}Al_{0.32}Mg_{0.04}]O_{20}(OH)_{2.93}$$

and its supercells should contain 7.8 H^+ which is very close to 8. As sorbed protons migrate from the interlayer space to the octahedral sheet to compensate undersaturated bordering O atoms, the structural formula can be finally written:

$$Na_{1.30}[Si_{7.22}Al_{0.78}][Fe^{2+}_{3.65}Al_{0.32}Mg_{0.04}]O_{17.93}(OH)_5$$

For this model, N_{Fe1} = 4.3–4.4, the proportion of short Fe-Fe2 distances amounts to 35% and the occupancy of M1 sites is 26%. All these values are within the precision of P-EXAFS and diffraction results, and one may consider that this model accounts reasonably well for the whole set of structural data obtained for GR, and provides a reasonable description of the idealized structure of the octahedral sheet for totally reduced Garfield nontronite. The general consistency of this structural model must be emphasized as it strengthens our considerations of the general mechanism of the reduction of Fe^{3+} to Fe^{2+} as well as to the compensation of the layer charge proposed in the present study. It is shown in Drits and Manceau (2000), that this structural model provides a rationale to explain quantitatively the change of the physico-chemical properties of smectites as a function of the reduction rate.

ACKNOWLEDGMENTS

E. Curti, A. Scheidegger, and S. Traina are acknowledged for their review, and R.A. Eggleton is thanked for his editorial handling. The authors thank the staff at LURE for operating the synchrotron facility, and specifically Agnès Traverse for running the D42 spectrometer. The authors also acknowledge with appreciation the assistance of Laibin Yan in collecting infrared spectra of Garfield nontronite. A.M. acknowledges the University of Illinois at Urbana-Champaign

for a George A. Miller Endowment fellowship. D.C. acknowledges H.R. Wenk and M. Pernet for access to the texture experiments at the Department of Geology and Geophysics, University of California-Berkeley, and Laboratoire de Cristallographie, Grenoble, France, respectively. W.G. acknowledges the French Consulate for a bourse Chateaubriand. J.W.S. acknowledges the Illinois Council for Food and Agricultural Research and V.A.D. the Russian Science Fundation for partial funding of this study.

REFERENCES CITED

Angell, C.L. and Schaffer, P.C. (1965) Infrared spectroscopic investigations of zeolites and adsorbed molecules. I. Structural OH groups. Journal of Physical Chemistry, 65, 3463–3470.

Bailey, S.W. (1984) Micas. In Mineralogical Society of America Reviews in Mineralogy, 13.

Barshad, I. and Kishk, F.M. (1968) Oxidation of ferrous iron in biotite and vermiculite alters fixation and replaceability of potassium. Science, 162, 1401–1402.

Besson, G. and Drits, V.A. (1997) Refined relationships between chemical composition of dioctahedral fine-grained mica minerals and their infrared spectra within the OH stretching region. Part II: The main factors affecting OH vibrations and quantitative analysis. Clays and Clay Minerals, 45, 170–183.

Brindley, G.W. and Brown, G. (1980) Crystal structures of clay minerals and their X-ray identification, 495 p. Mineralogical Society, London.

Brindley, G.W. and LeMaitre, J. (1987) Thermal, oxidation and reduction reaction of clay minerals. In A.C.D. Newman, Ed., Chemistry of Clays and Clay Minerals, 6, 319–370. Mineralogical Society Monograph, London.

Brown, I.D. (1976) On the geometry of O-H....O hydrogen bonds. Acta Crystallographica, A32, 24–31.

Brown, I.D. (1981) The bond-valence method: An empirical approach to chemical structure and bonding. In M. O'Keefe and A. Navrotsky, Eds., Structures and Bonding in Crystals, II, p. 1–30. Academic Press, New York.

Brown, I.D. and Shannon, R.D. (1973) Empirical bond-strength-bond-length curves for oxides. Acta Crystallographica, A29, 266–282.

Burns, R.G. and Strens, R.G.J. (1966) Infrared study of the hydroxyl bands in clinoamphiboles. Science, 153, 890–892.

Douglas, B., McDaniel, D., and Alexander, J. (1994) Concepts and models of inorganic chemistry, 928 p. John Wiley and Sons, New York.

Drits, V.A. and Manceau, A. (2000) A new model for the reduction mechanism of Fe (III) to Fe (II) in dioctahedral smectites. Clays and Clay Minerals, in press.

Drits, V.A. and Tchoubar, C. (1990) X-ray diffraction by disordered lamellar structures: Theory and applications to microdivided silicates and carbons, 371 p. Springer Verlag, Berlin.

Drits, V.A., Plançon, A., Sakharov, B.A., Besson, G., Tsipursky, S.I., and Tchoubar, C. (1984) Diffraction effects calculated for structural models of K-saturated montmorillonite containing different types of defects. Clay Minerals, 19, 541–561.

Drits, V.A., Besson, G., and Muller, F. (1995) An improved model for structural transformation of heat-treated aluminous dioctahedral 2:1 layer silicates. Clays and Clay Minerals, 43, 718–731.

Egashira, K. and Ohtsubo, M. (1983) Swelling and mineralogy of smectites in paddy soils derived from marine alluvium, Japan. Geoderma, 29, 119–127.

Ernsten, V., Gates., W.P., and Stucki, J.W. (1996) Microbial reduction of structural iron in clays — A renewable source of reduction capacity. Journal of Environmental Quality, 27, 761–766.

Farges, F., Brown, G.E., and Rehr, J.J. (1997) Ti K-edge XANES studies of Ti coordination and disorder in oxide compounds: Comparison between theory and experiment. Physical Review, 56, 1809–1819.

Farmer, V. C. (1974) The layer silicates. In V. C. Farmer (ed.), Infrared Spectra of Minerals, p. 339–340. Mineralogical Society, London.

Gates, W.P., Wilkinson, H.T., and Stucki, J.W. (1993) Swelling properties of microbially reduced ferruginous smectite. Clays and Clay Minerals, 41, 360–364.

Gates, W.P., Jaunet, A.M., Tessier, D., Cole, M.A., Wilkinson, H.T., and Stucki, J.W. (1998) Swelling and texture of iron-bearing smectites reduced by bacteria. Clays and Clay Minerals, 46, 487–497.

Goodman, B.A., Russell, J.D., Fraser, A.R., and Woodhams, F.W.D. (1976) A Mössbauer and IR spectroscopic study of the structure of nontronite. Clays and Clay Minerals, 24, 53–59.

Huo, D. (1997) Infrared study of oxidized and reduced nontronite and Ca-K competition in the interlayer. Ph.D. dissertation, 139 p. University of Illinois, Urbana, Illinois.

Komadel, P. and Stucki, J.W. (1988) The quantitative assay of minerals for Fe^{2+} and Fe^{3+} using 1,10-phenanthroline. III. A rapid photochemical method. Clays and Clay Minerals, 36, 379–381.

Lear, P.R. and Stucki, J.W. (1985) The role of structural hydrogen in the reduction and reoxidation of iron in nontronite. Clays and Clay Minerals, 33, 539–545.

———(1989) Effects of iron oxidation state on the specific area of nontronites. Clays and Clay Minerals, 37, 547–552.

Lee, J.H. and Guggenheim, S. (1981) Single crystal X-ray refinement of pyrophyllite-1Tc. American Mineralogist, 66, 350–357.

Manceau, A. and Gates, W. (1997) Surface structural model for ferrihydrite. Clays and Clay Minerals, 448–460.

Manceau, A., Bonnin, D., Kaiser, P., and Frétigny, C. (1988) Polarized EXAFS of biotite and chlorite. Physics and Chemistry of Minerals, 16, 180–185.

Manceau, A., Bonnin, D., Stone, W.E.E., and Sanz, J. (1990) Distribution of Fe in the octahedral sheet of trioctahedral micas by polarized EXAFS. Comparison with NMR results. Physics and Chemistry of Minerals, 17, 363–370.

Manceau, A., Chateigner, D., and Gates, W.P. (1998) Polarized EXAFS, distance-valence least-squares modeling (DVLS) and quantitative texture analysis approaches to the structural refinement of Garfield nontronite. Physics and Chemistry of Minerals, 25, 347–365.

Manceau, A., Schlegel, M., Chateigner, D., Lanson, B., Bartoli, C., and Gates, W.P. (1999) Application of polarized EXAFS to fine-grained layered minerals. In D. Schulze, P. Bertsch and J. Stucki, Eds., Synchrotron X-ray Methods in Clay Science. Clay Mineral Society of America, 9, 69–114.

Manceau, A., Lanson, B., Drits, V.A., Chateigner, D., Gates, W.P., Wu, J., Huo, D.F., and Stucki, J.W. (2000) Oxidation-reduction mechanism of iron in dioctahedral smectites. I. Structural chemistry of oxidized nontronite references. American Mineralogist, 85, 133–153.

O'Day, P.A., Rehr, J.J., Zabinsky, S.I., and Brown, G.E., Jr. (1994) Extended x-ray absorption fine structure (EXAFS) analysis of disorder and multiple-scattering in complex crystalline solids. Journal of the American Chemical Society, 116, 2938–2949.

Pauling, L. (1929) The principles determining the structure of complex ionic crystals. Journal of the American Chemical Society, 51, 1010–1026.

Plançon, A. (1981) Diffraction by layer structure containing different kinds of layers and stacking faults. Journal of Applied Crystallography, 14, 300–304.

Rehr, J.J., Mustre de Leon, J., Zabinsky, S.I., and Albers, R.C. (1991) Theoretical x-ray absorption fine structure standards. Journal of the American Chemical Society, 113, 5135–5145.

Roth, C.B. and Tullock, R.J. (1973) Deprotonation of nontronite resulting from chemical reduction of structural ferric iron. In J.M. Serratosa, Ed., Proceeding International Clay Conference, p. 107–114. Division Ciencas C.S.I.C., Madrid.

Rozenson, I. and Heller-Kallai, L. (1978) Reduction and oxidation of Fe^{3+} in dioctahedral smectite. 3: Oxidation of octahedral iron in montmorillonite. Clays and Clay Minerals, 26, 88–92.

Russell, J.D., Goodman, B.A., and Fraser, A.R. (1979) Infrared and Mössbauer studies of reduced nontronites. Clays and Clay Minerals, 27, 63–71.

Sakharov, B.A., Naumov, A.S., and Drits, V.A. (1982a) X-ray intensities scattered by layer structure with short range ordering parameters S≥1 and G≥1. Dokladi Akademie Naukia SSSR, 265, 871–874.

———(1982b) X-ray diffraction by mixed-layer structures with random distribution of stacking faults. Dokladi Akademie Naukia SSSR, 265, 339–343.

Slonimskaya, M., Besson, G., Dainyak, L.G., Tchoubar, C., and Drits, V.A. (1986) Interpretation of the IR spectra of celadonites and glauconites in the region of OH-stretching frequencies. Clay Minerals, 21, 377–388.

Stern, E.A. and Kim, K. (1981) Thickness effect on the extended x-ray absorption fine structure amplitude. Physical Review, B23, 3781–3787.

Stubican, V. and Roy, R. (1961) A new approach to assignment of infra-red absorption bands in layer-structure silicates. Zeitschrift für Kristallographie, 15, 200–214.

Stucki, J.W. (1988) Structural iron in smectites. In J.W. Stucki, B.A. Goodman and U. Schwertmann, Eds., Iron in Soils and Clay Minerals, 217, p. 625–676. Riedel Publishing Company.

Stucki, J.W. and Roth, C.B. (1976) Interpretation of infrared spectra of oxidized and reduced nontronite. Clays and Clay Minerals, 24, 293–296.

———(1977) Oxidation-reduction mechanism for structural iron in nontronite. Soil Science Society of America Journal, 41, 808–814.

Stucki, J.W. and Tessier, D. (1991) Effects of iron oxidation state on the structural order of Na-nontronite. Clays and Clay Minerals, 39, 137–143.

Stucki, J.W., Golden, D.C., and Roth, C.B. (1984) Effects of reduction and reoxidation of structural iron on the surface charge and dissolution of dioctahedral smectites. Clays and Clay Minerals, 32, 350–356.

Stucki, J.W., Komadel, P., and Wilkinson, H.T. (1987) The microbial reduction of structural iron(III) in smectites. Soil Science Society of America Journal, 51, 1663–1665.

Takeda, H. and Ross, M. (1975) Mica polytypism: Dissimilarities in the crystal structures of coexisting 1M and 2M1 biotite. American Mineralogist, 60, 1030–1040.

Teo, B.K. (1986) EXAFS: Basic principles and data analysis, 349 p. Springer-Verlag, Berlin.

Wilkins, R.W.T. and Ito, J. (1967) Infrared spectra of some synthetic talcs. American Mineralogist, 52, 1649–1661.

MANUSCRIPT RECEIVED AUGUST 3, 1998
MANUSCRIPT ACCEPTED AUGUST 15, 1999
PAPER HANDLED BY R.A. EGGLETON